Chapter 1 Introduction

1-1 Background

Half century ago, physicists have known the dispersion relation in a electronic system due to periodic electric potential structure. Like mentioned above, in 1987, Eli Yablonovitch (Bell Communication) and Sajeev John (Princeton University) addressed the same concept of photonic crystal [1-3]. In this artificial material, we let the dielectric constant arranged periodically, and in this kind of structure the EM wave will have interference caused by incident and reflective waves when it passes the structure, hence the band gap phenomenon happens. In the decade, the developments and applications of the photonic crystal have been discussed hotly, and many famous scientific bulletins pointed the potential of it. By controlling the ability of electronics, semi-conductors have improved the evolution of communication and computer, and now we believe if we could control photons like electrons, another evolution will come in the future. Photonic crystals consist of two or more dielectric constant materials to form a periodic structure; and we can distinguish them one, two and three dimensional photonic crystals shown in fig. 1-1 [3]
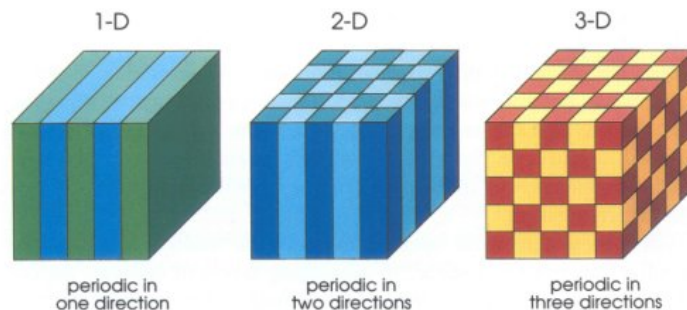
Fig. 1-1 An example of different dimensions photonic crystal; the different colors represent the different dielectric constants.

One dimensional photonic crystal is the simplest possible structure, as shown in

fig. 1-2 [3], and it has a multi-layers structure which is studied by Lord Rayleigh [4-5]. This structure is a Bragg stack and used to be a perfect mirror for light in a specific frequency which causes a photonic band gap and its reflectivity could be above 99%. This structure is commonly used in all optical experiments like Bragg reflector.
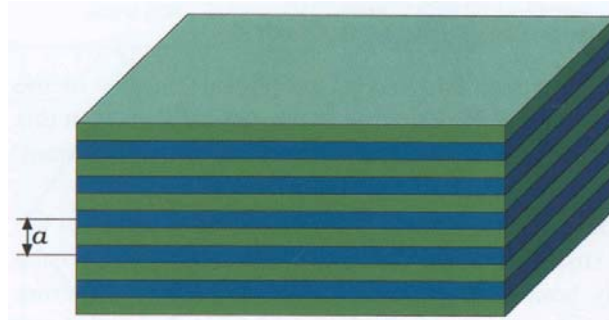
Fig. 1-2 One-dimensional photonic crystal and a is the lattice constant.

The two dimensional photonic crystal, shown in fig. 1-3, is the hottest topics nowadays, and there are many applications have been shown as high-Q cavities [6-7] and waveguide device which includes electro-optical switch [8], MZ interferometer [9], and multiplexers/demultiplexers [10-11].
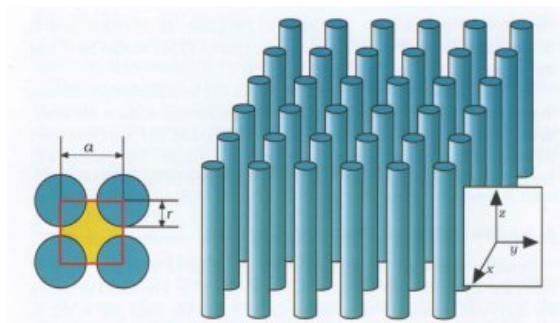
Fig. 1-3 An example of two dimensional photonic crystal.
This is a square lattice of dielectric columns with
radius r and lattice constant a. This material is
homogenous in the z direction and periodic in the
x and y direction.

By removing some dielectric materials, PCs waveguides could be fabricated,

and different kind of the structures will make different band diagrams for TE and TM wave (This will be discussed in chapter 2-1). In fact, the experiment has proved we can control the size of the defect and refractive index of the material to construct the device we want. A photonic crystal waveguide is made by removing one or more line materials, and the wide of the channel will cause single or multi-mode like convention waveguide. The PCs waveguide plays a very important role in optical communication like wires in electronic system. In conventional waveguide like optical fiber the transmission is constricted when the angle of the corner is too large (the curvature radius is too small), however, the PCs waveguides could solve this problem even in 120° turn called zigzag waveguides. Another important point is the micro-cavities on photonic crystal. We can introduce some defect called point defect on PCs; light wave will vibrate in the small cavity. Combining this with light-emitting diodes will highly enhance the photo-emission [12]; and the PCs cavity is crucial for constructing a high-Q cavity. There are still many researches in two dimensional photonic crystals, for example, low group velocity, coupling mechanism, and near-field image.
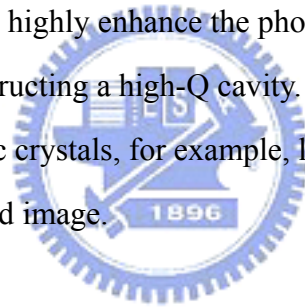
1-2 Motivation

In the fifty years recently, the technology of semi-conductor has a great advancement and brings convenience for human being. But when the device and circuit have become smaller and dense, many restrictions has emerged, like interference between devices, signal delay caused by dense circuit, heat storage and so on. Therefore many scholars try to use the photons to replace the electrons. There many advantages of photons, the fast velocity, neutrality, and wider frequency band.

Now the optical communication has been realized by photonic crystals. In my thesis, the photonic crystal waveguide is focused to study its properties, and many interesting behaviors like coupling/decoupling, ultra-coupling length, and impendence math in corner are shown in chapter 3. Nevertheless, we focus on the physical characteristics of photonic crystal waveguides and optical device such as wave division multiplexing (WDM). In this topic the plan wave expansion method (PWE) and finite difference time domain method (FDTD) are used to calculate their band-solving and real space wave transmission, respectively.

1-3 Applications of photonic crystals

A photonic crystal is a artificial material with periodic refractive index. And there are two commonly used structures called square and triangular lattice; they have different band structures for TM and TE wave defined in fig. 1-4. And the two band diagrams are shown in fig. 1-5.
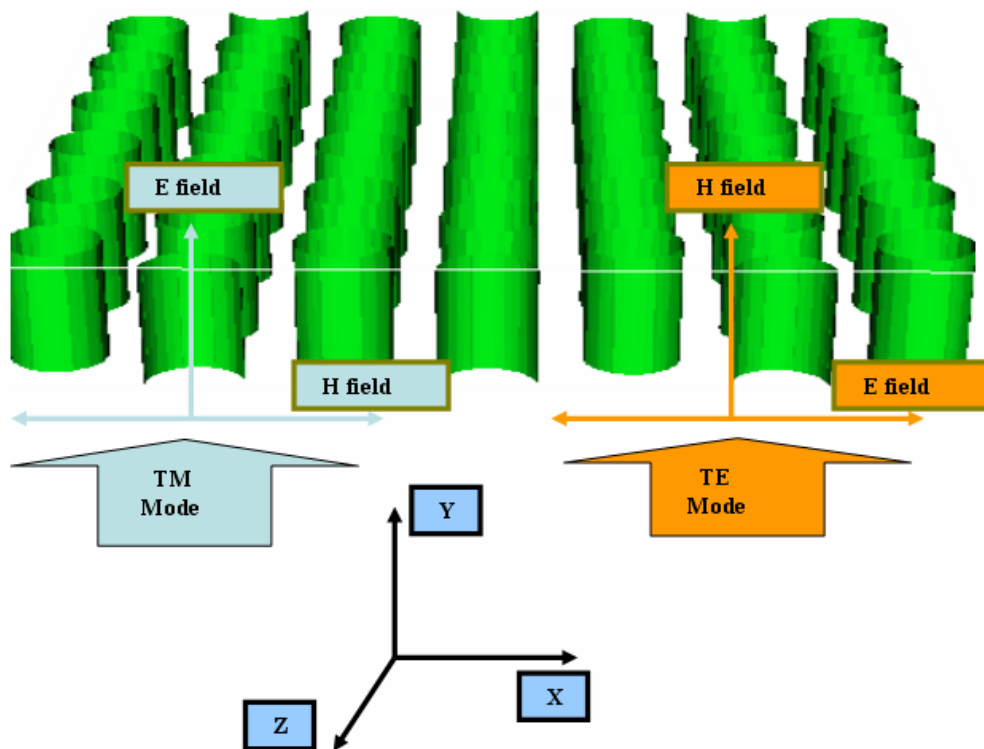
Fig. 1-4 The TE wave is the H field parallel to the y-axis; The TM wave is the E field parallel to the y-axis.

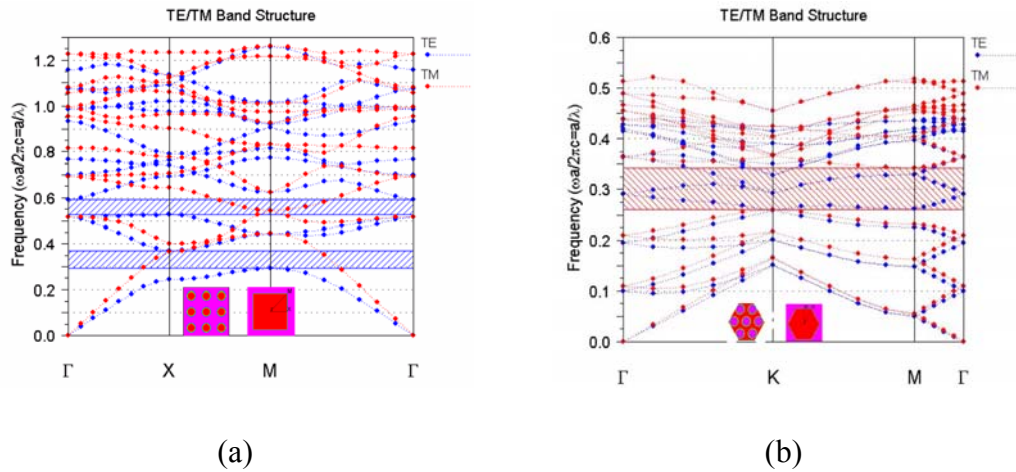(a)   (b)

Fig. 1-5 The band diagrams of the two structures (a) the square lattice and (b)

the triangular lattice. The insets are unit cell and first brillouin zone. The

square lattice structure has rod materials in the air background; the

triangular lattice structure has air holes in the materials background.

The basic device is a line defect photonic crystals waveguide; the structure is by

removing one line or more lines of air holes or dielectric materials in the photonic

crystal (fig. 1-6) [13]. For single mode design, the slab thickness is usually below 0.3

μm; the width of the channel is usual a single line defect. And in the vertical

direction the refractive index confinement is used to strict the light; in the in-plane
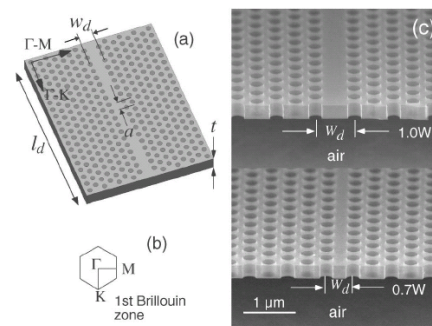
direction the Bragg reflection is used.

Fig. 1-6 One missing-hole line defects of the hexagonal air holes (a) Schematic of

samples, (b) reciprocal-space representation, (c) SEM of fabricated PC

slabs.

6

Other devices like Y-branch power splitter and coupling/decoupling switch shown in below (Fig. 1-7 and 1-8) [14-15] are also important and be discussed later.
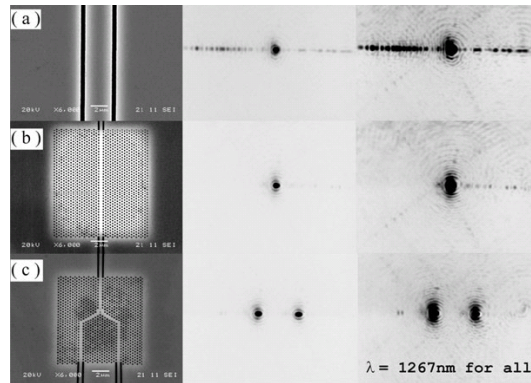

Fig. 1-7 SEM graphs of (a) a conventional ridge waveguide with 3 μm, (b) a W1 waveguide and (c) a Y-junction. The graphs in the middle and right are input power is 0.05mW and 0.5mW, and λ is 1267 nm of the TE_{00} wave.
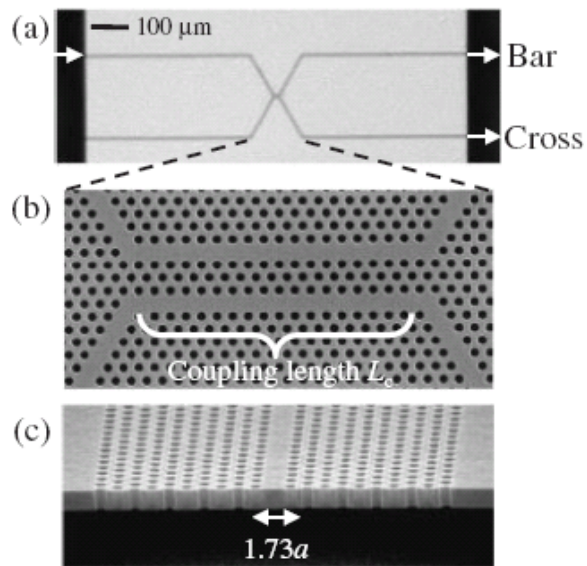

Fig. 1-8 2D-PC slab directional coupler combined with bent waveguides. (a) Optical microscope image and (b) SEM picture. (c) The cleaved facet of the waveguide.

1-4 Thesis overview

      In my thesis, we divided our text into five chapters. We have introduced the physical properties and background of the photonic crystal and some devices in this chapter. In the chapter 2 we have the introductions about PWE method, FETD method, and coupling mechanism. And then we will show the results of the simulations of some PCs applications as line-defect waveguide, coupling-type switch in the chapter 3. Finally, the measurement and conclusion will be shown in the chapter 4 and 5.

Chapter 2 Theory of photonic crystal simulation and coupling mechanism

In this chapter, the analyses to electromagnetic wave in photonic crystal start from four Maxwell equations.

$$\nabla \cdot D = \rho$$
$$\nabla \cdot B = 0$$
$$\nabla \times E = -\frac{1}{C_0}\frac{\partial B}{\partial t} \qquad\qquad (2\text{-}1)$$
$$\nabla \times H = \frac{1}{C_0}\frac{\partial D}{\partial t} + J$$

As we know E, H, D and B are electric field, magnetic fields, electric displacement, and magnetic induction. Here ρ and J are charge density and current density, and our case is free charge hence ρ and J are zero. In the simulation of photonic crystal, we use the plane wave expansion to calculate the band diagram and FDTD to get power transmission.

2-1 Plane wave expansion

Plane wave expansion is a frequency domain method; it could show the band diagram, the relation between the frequency and propagation constant, of a photonic crystal structure. As we know, in the electronic system, the Schrödinger equation is used to calculate the band; like above Maxwell equations play an important role for light propagation. In photonic crystals with periodic structures, we have the dielectric function in real space:

$$\varepsilon(\vec{r}) = \varepsilon(\vec{r} + a_i) \qquad i = 1,2,3 \tag{2-1.1}$$

$$\vec{G} = l_1\vec{b}_1 + l_2\vec{b}_2 + l_3\vec{b}_3$$

(2-1.2)

$$a_i \cdot b_j = 2\pi\delta_{ij} \tag{2-1.3}$$

, hence the coulomb potential of the electronic system is substituted by the dielectric index $\varepsilon(\vec{r})$ for light wave in photonic crystal. Here a_i is the primitive lattice vectors in photonic crystals, and $\vec{G}$ is the reciprocal vector the same in solid state as shown in fig. 2-1.1~2,
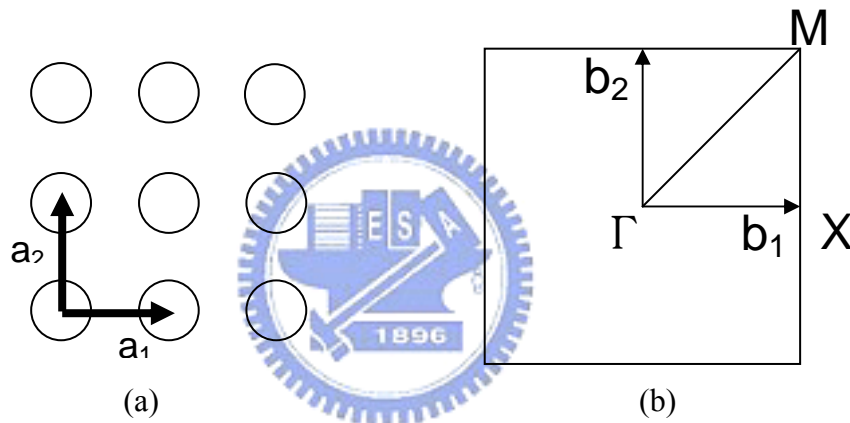

(a)   (b)

Fig. 2-1.1 (a) The real space of the square lattice. (b) The first brillouin zone of the square lattice.
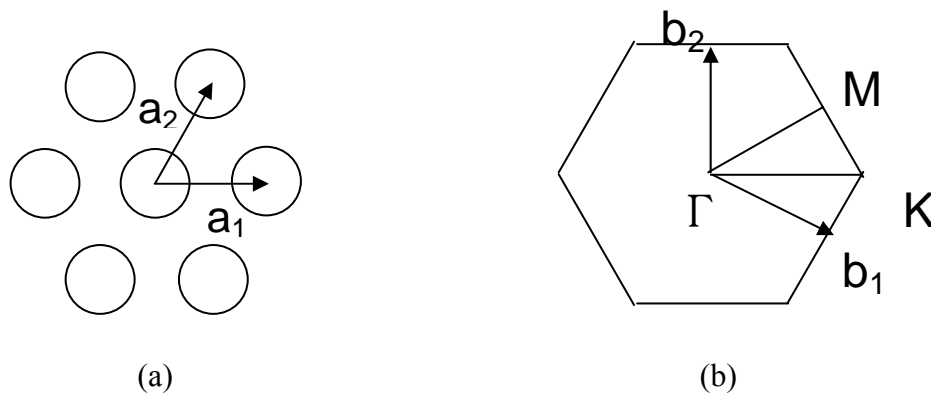

(a)   (b)

Fig. 2-1.2 (a) The real space of the triangular lattice. (b) The first Brillouin zone of the triangular lattice.

where $\{l_i\}$ are arbitrary integers, and δ_{ij} is the Kronecker's delta function. And the $\varepsilon^{-1}(\bar{r})$ can be written as the Fourier expansion:

$$\frac{1}{\varepsilon(\bar{r})} = \sum_G \kappa(\bar{G}) \exp(i\bar{G} \cdot \bar{r}) \qquad (2\text{-}1.4)$$

It's because that the refractive index is real, the $\kappa(-\bar{G}) = \kappa^*(\bar{G})$. And the wavefunction for an electric or magnetic field could be written as:

$$\Theta \bar{E}(\bar{r}) \equiv \frac{1}{\varepsilon(\bar{r})} \nabla \times \left\{ \nabla \times \bar{E}(\bar{r}) \right\} = \left(\frac{\omega}{c} \right)^2 \bar{E}(\bar{r}) \qquad (2\text{-}1.5)$$

$$\Theta \bar{H}(\bar{r}) \equiv \nabla \times \left\{ \frac{1}{\varepsilon(\bar{r})} \nabla \times \bar{H}(\bar{r}) \right\} = \left(\frac{\omega}{c} \right)^2 \bar{H}(\bar{r}) \qquad (2\text{-}1.6)$$

In Eq. 2-1.1, the dielectric function ε is a periodic function of the spatial coordinate, hence we could use Bloch's theorem in Eqs. (2-1.5) and (2-1.6). We can obtain the following eigenvalue equations for the Fourier expansion:

$$-\sum_{G'} \kappa(G - G')\left\{(k + G) \times (k + G') \times E_{kn}(G')\right\} = \frac{\omega_{kn}^2}{c^2} E_{kn}(G) \qquad (2\text{-}1.7)$$

$$-\sum_{G'} \kappa(G - G')\left\{(k + G) \times (k + G') \times H_{kn}(G')\right\} = \frac{\omega_{kn}^2}{c^2} H_{kn}(G) \qquad (2\text{-}1.8)$$

here, ω_{kn} is the eigenvalue of the specific $E_{kn}(r)$ and $H_{kn}(r)$. We could obtain the dispersion relation of the eigenmodes by solving these two sets of equations numerically. And this numerical method based on the Fourier expansion of the

electromagnetic field and dielectric function is called plane-wave expansion method.

2-2 Finite-difference time-domain method (FDTD) [16]

In 1966 Yee [17] proposed finite-difference time-domain (FDTD) technique to solve Maxwell's cur equations, and FDTD method is general class of a differential time domain method. Hence FDTD method is usually used in the simulation of the behavior of the electromagnetic wave in a photonic crystal structure. For differential Maxwell's equations, we could take the functions to replace the differential functions, expand them and finally we obtain the algorithm of the FDTD method. And FDTD is usually used to study the characteristic of the electromagnetic waves in different dielectric materials, metal, and etc.

When we obtain the differential form of Maxwell's equations, it could be regarded that the time derivate E field is relate to Curl of the H field. As we know the rate of the change about the E field is associate with the change of the H field in the space. And it's similar for H field. We could use Fig. 2.2-1 to represent the relationship between the E and H field. Here the new value of the E field is related to the old E value and the differential H field value.
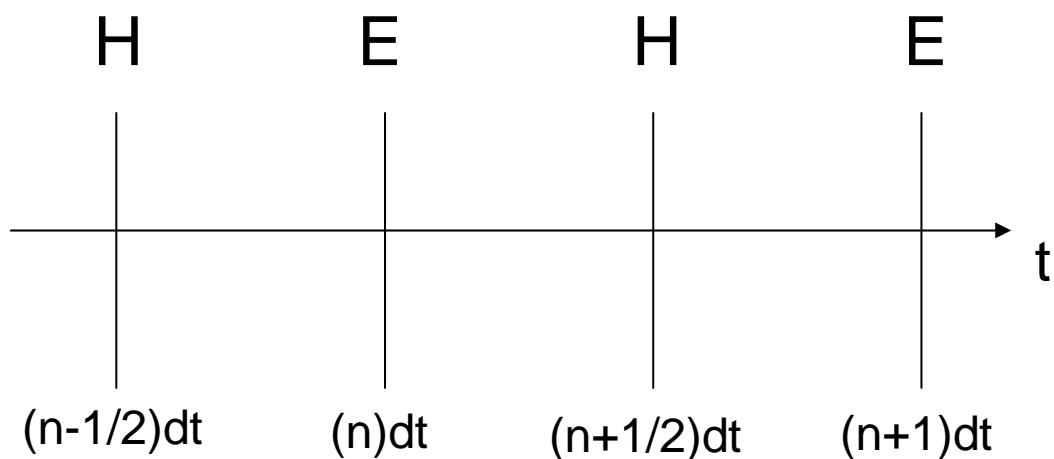

Fig. 2-2.1 The relation between the E and H field in time.

2-2.1 Maxwell's equations and Yee's cell

In FDTD simulation, Faraday's and Amp's laws will be written as the form:

$$\nabla \times H = \frac{\partial D}{\partial t} + \boldsymbol{J}_e \qquad (2\text{-}2.1)$$

$$\nabla \times E = -\frac{\partial B}{\partial t} - \boldsymbol{J}_m \qquad (2\text{-}2.2)$$

here, J_e is the electric current source, and J_m is magnetic current source, but indeed in nature there is no magnetic monopole in consequence $J_m = 0$. The values about the all variable parameters are shown below Tab. 2-2.1.

Tab. 2-2.1 The all values of electromagnetic wave.

$D = \varepsilon E$	$J_e = \sigma E$
$B = \mu H$	$J_m = sH$
E : Electric field (V/m)	H : Magnetic field (A/m)
D : Electric displacement (C/m^2)	B : Magnetic induction (Wb/m^2)
J_e : Electric current density (A/m^2)	J_m : Magnetic current density (V/m^2)
$\varepsilon = \varepsilon_0 \varepsilon_r$: Dielectric constant	$\mu = \mu_0 \mu_r$: Magnetic constant
$\varepsilon_0 = 8.85 * 10^{-12}$ F/m	$\mu_0 : 4*pi*10^{-7}$ H/m
σ : Electronic conduct constant	

If we expand Eq. (2-2.1~2) at rectangular coordinate system, Eq. (2-2.3) is obtained. In numerical calculation, the differential functions in Eq. (2-2.1~2) have to change to the difference functions. The time and space are divided to form a discrete time and space lattice point. Let f (x, y, z, t) is the function of E or field, we could

used a integer, n, to represent the time and (i, j, k) represent the space. Hence the
approximate central difference functions could be written as the forms in Eq. (2-2.4).

$$\frac{\partial H_z}{\partial y} - \frac{\partial H_y}{\partial z} = (\sigma + \varepsilon_0 \varepsilon_r \frac{\partial}{\partial t})E_x$$

$$\frac{\partial H_x}{\partial z} - \frac{\partial H_z}{\partial x} = (\sigma + \varepsilon_0 \varepsilon_r \frac{\partial}{\partial t})Ey$$

$$\frac{\partial H_y}{\partial x} - \frac{\partial H_x}{\partial y} = (\sigma + \varepsilon_0 \varepsilon_r \frac{\partial}{\partial t})E_z$$

$$\frac{\partial E_y}{\partial z} - \frac{\partial E_z}{\partial y} = (s + \mu_0 \mu_r \frac{\partial}{\partial t})H_x \qquad (2\text{-}2.3)$$

$$\frac{\partial E_z}{\partial x} - \frac{\partial E_x}{\partial z} = (s + \mu_0 \mu_r \frac{\partial}{\partial t})Hy$$

$$\frac{\partial E_x}{\partial y} - \frac{\partial E_y}{\partial x} = (s + \mu_0 \mu_r \frac{\partial}{\partial t})H_z$$

$$\frac{\partial f(x,y,z,t)}{\partial x} = \frac{f^n(i+1/2, j,k) - f^n(i-1/2, j,k)}{dx}$$

$$\frac{\partial f(x,y,z,t)}{\partial y} = \frac{f^n(i, j+1/2,k) - f^n(i, j-1/2,k)}{dy}$$

$$\qquad (2\text{-}2.4)$$

$$\frac{\partial f(x,y,z,t)}{\partial z} = \frac{f^n(i, j,k+1/2) - f^n(i, j,k-1/2)}{dz}$$

$$\frac{\partial f(x,y,z,t)}{\partial y} = \frac{f^{n+1/2}(i, j,k) - f^{n-1/2}(i, j,k)}{dy}$$

For a proper dividing in space, we can get a Yee's cell Fig. 2-2.2 to describe the
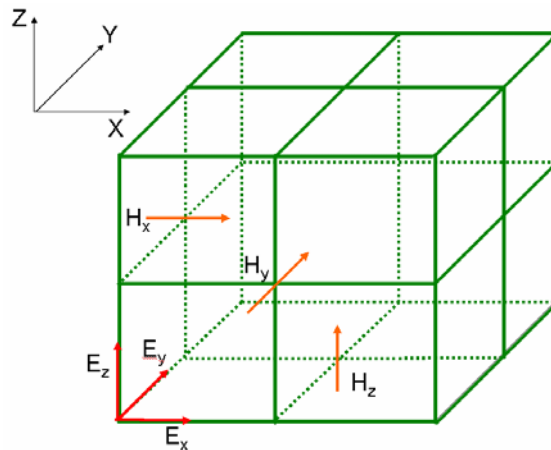Faraday's law and Amp's law.

Fig. 2-2.2 The divide in space.

Finally in order to reduce the error in calculation, the size of the space point is usually set as λ/20:

$$dx \leq \frac{\lambda}{20} \qquad (2\text{-}2.5)$$

, and the time point also has the similarity :

$$dt \leq \frac{1}{c\sqrt{(\frac{1}{dx})^2 + (\frac{1}{dy})^2 + (\frac{1}{dz})^2}} \qquad (2\text{-}2.6)$$

If these conditions are not cared, the distortion of the wave will happen, called space dispersion, with the increase in time. In conclusion, the intervals of the points of the space and the time have to cut small enough to prevent the distortions.

2-2.2 One-dimensional simulation with FDTD method

Here we start with the simple one-dimensional differential equations. The Maxwell's curl equations for time-dependent in free space are :

$$\frac{\partial \vec{E}}{\partial t} = \frac{1}{\varepsilon_0} \nabla \times \vec{H} \qquad (2\text{-}2.7)$$

$$\frac{\partial \vec{H}}{\partial t} = -\frac{1}{\mu_0} \nabla \times \vec{E} \qquad (2\text{-}2.8)$$

In Eq. 2.2-2a, $\vec{E}$ and $\vec{H}$ are the three dimensional vector, but now we only consider in the one-dimensional case, hence the Eq. 2.2-2a will becomes (the wave is toward the z direction):

$$\frac{\partial E_x}{\partial t} = -\frac{1}{\varepsilon_0} \nabla \times H_y \tag{2-2.9}$$

$$\frac{\partial H_y}{\partial t} = -\frac{1}{\mu_0} \nabla \times E_x \tag{2-2.10}$$

And then we use the central difference approximation mentioned in Eq. (2-2.9~10) for both the temporal and spatial derivation.

$$\frac{E_x^{n+1/2}(k) - E_x^{n-1/2}(k)}{\Delta t} = -\frac{1}{\varepsilon_0} \frac{H_y^n(k+1/2) - H_y^n(k-1/2)}{\Delta z} \tag{2-2.11}$$

$$\frac{H_y^{n+1}(k+1/2) - H_y^n(k+1/2)}{\Delta t} = -\frac{1}{\mu_0} \frac{E_y^{n/1/2}(k+1) - H_y^{n+1/2}(k)}{\Delta z} \tag{2-2.12}$$

In Eq. (2-2.11), the "n" is denoted a time $t = \Delta t * n$, and the n+1 represents the next time step. The "k" is the distance $z = \Delta z * k$. In these two equations, the E and H fields are interleaved with each other in both space and time. In Eq. (2-2.11) the H field is denoted the time "n", and it's interleaved in n+1/2 and n-1/2 of the E field. The similar in space E is denoted the space "k" interleaved in k+1/2 and k-1/2 of the H field. We can rearranged the Eq. (2-2.11~12) to

$$E_x^{n+1/2}(k) = E_x^{n-1/2}(k) - \frac{\Delta t}{\varepsilon_0 \cdot \Delta z} [H_y^n(k+1/2) - H_y^n(k-1/2)] \tag{2-2.13}$$

$$H_x^{n+1}(k+1/2) = H_x^n(k+1/2) - \frac{\Delta t}{\varepsilon_0 \cdot \Delta z} [E_y^{n+1/2}(k+1) - E_y^{n+1/2}(k)] \tag{2-2.14}$$

16

Then making some change of the variables:

$$\widetilde{E} = \sqrt{\frac{\varepsilon_0}{\mu_0}} E \qquad (2\text{-}2.15)$$

Hence the Eq. (2-2.15) could be substituted to Eq. (2-2.13~14), we obtain :

$$\widetilde{E}_x^{n+1/2}(k) = \widetilde{E}_x^{n-1/2}(k) - \frac{1}{\sqrt{\varepsilon_0 \mu_0}} \frac{\Delta t}{\Delta z} [H_y^n(k+1/2) - H_y^n(k-1/2)] \qquad (2\text{-}2.16)$$

$$H_x^{n+1}(k+1/2) = H_x^{n-1/2}(k+1/2) - \frac{1}{\sqrt{\varepsilon_0 \mu_0}} \frac{\Delta t}{\Delta z} [\widetilde{E}_y^{n+1/2}(k+1) - \widetilde{E}_y^{n+1/2}(k)] \qquad (2\text{-}2.17)$$

For the reason to be stability of the FDTD method, if we chose a cell size Δz, the time step can be determined by

$$\Delta t = \frac{\Delta x}{2c_0} . \qquad (2\text{-}2.18)$$

where c_0 is the light speed in free space. Eq. (2-2.18) tells us that the electromagnetic wave can't be faster than the light speed. Propagating a distance needs a minimum time of $\Delta t = \frac{\Delta z}{c_0}$. And in a 2-D system the requirement, $\Delta t = \frac{\Delta z}{\sqrt{2}c_0}$, is needed.

Similarly, the simulation in a 3-D system needs $\Delta t = \frac{\Delta z}{\sqrt{3}c_0}$. This is called "Courant Condition" [18~19]:

$$\Delta t \leq \frac{\Delta z}{\sqrt{n}c_0} \qquad (2\text{-}2.19)$$

where n is represented the dimension of the simulation.

2-2.3 Two dimensional formulation

Actually, we often use the 2-D simulation to replace the 3-D simulation in order
to save the time. Hence here we focus on the 2-D FDTD method and the boundary
condition. To start with the normalized Maxwell's equations again:

$$\frac{\partial \widetilde{D}}{\partial t} = \frac{1}{\sqrt{\varepsilon_0 \mu_0}} \nabla \times H \tag{2-2.20}$$

$$\widetilde{D}(\omega) = \varepsilon_r^*(\omega) \cdot \widetilde{E}(\omega) \tag{2-2.21}$$

$$\frac{\partial H}{\partial t} = -\frac{1}{\sqrt{\varepsilon_0 \mu_0}} \nabla \times \widetilde{E} \tag{2-2.22}$$

where $\widetilde{E} = \sqrt{\frac{\varepsilon_0}{\mu_0}} E$ and $\widetilde{D} = \sqrt{\frac{\varepsilon_0}{\mu_0}} D$. In the two dimensional case, we usually

divided the EM wave to two groups of three vectors. One is the transverse magnetic
(TM) mode, and the other is the transverse electric (TE) mode, which are defined by
the Fig. 1-4. The TE mode is composed of the E_y, H_x, and H_z. The other TM
mode, is composed of the H_y, E_x, and E_z. Here we focus on the TE mode for
example. Therefore, Eq. (2-2.20~22) are reduced to

$$\frac{\partial D_y}{\partial t} = -\frac{1}{\sqrt{\varepsilon_0 \mu_0}} (\frac{\partial H_z}{\partial x} - \frac{\partial H_x}{\partial z}) \tag{2-2.23}$$

$$D_y(\omega) = \varepsilon_r^*(\omega) \cdot E_y(\omega) \tag{2-2.24}$$

$$\frac{\partial H_x}{\partial t} = -\frac{1}{\sqrt{\varepsilon_0 \mu_0}} (\frac{\partial E_y}{\partial z}) \tag{2-2.24}$$

$$\frac{\partial H_z}{\partial t} = \frac{1}{\sqrt{\varepsilon_0 \mu_0}} \left(\frac{\partial E_y}{\partial x} \right) \tag{2-2.26}$$

The2-D systemic interleaving of the calculated fields is more complex the one-dimension. That's illustrated in Fig. 2.2-3
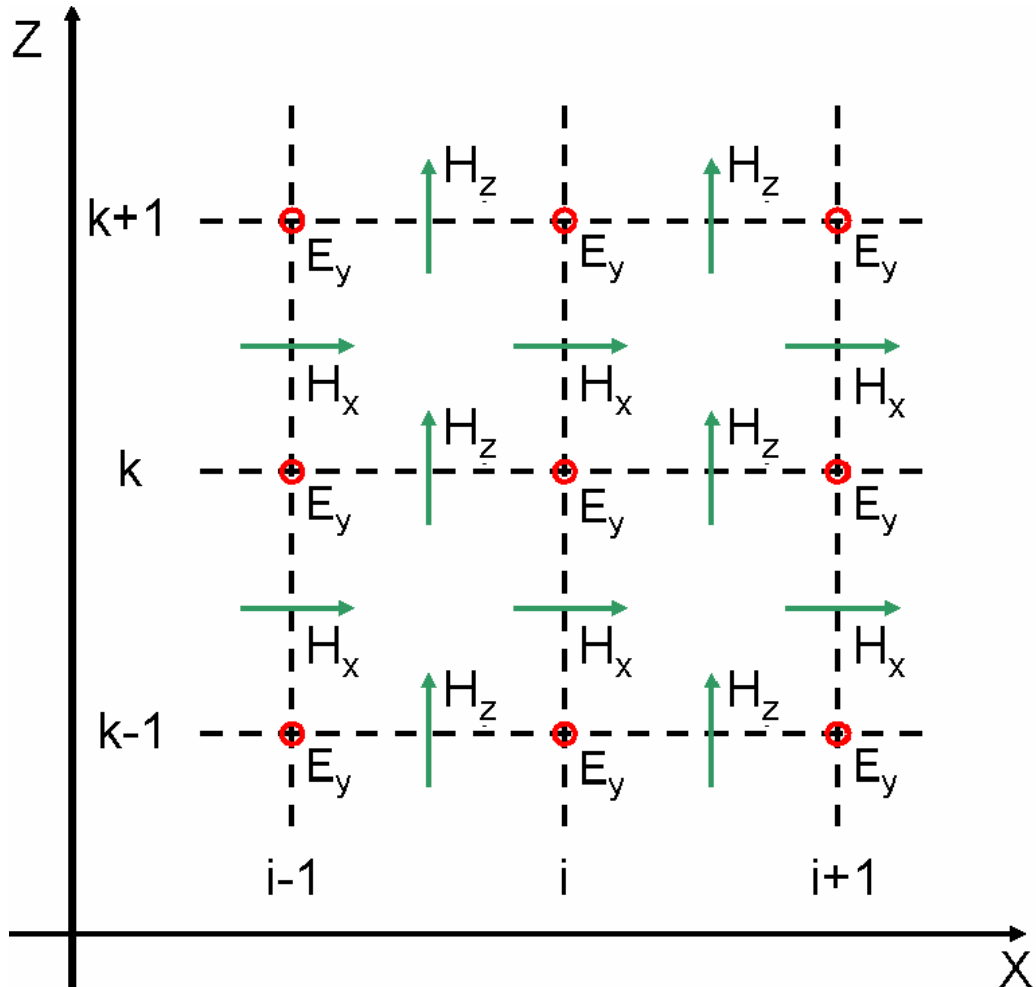

Fig. 2-2.3 Interleaving of the E and H fields for the two-dimensional TE formulation.

Then the differential Eq. (2.2-15a), (2.2-15c), and (2.2-15d) will be transferred into the difference equations:

$$\frac{D_y^{n+1/2}(i,k) - D_y^{n-1/2}(i,k)}{\Delta t} = \frac{1}{\sqrt{\varepsilon_0 \mu_0}} [(\frac{H_x^n(i,k+1/2) - H_x^n(i,k-1/2)}{\Delta z}) -$$

$$(\frac{H_z^n(i+1/2,k) - H_z^n(i-1/2,k)}{\Delta x})] \qquad (2\text{-}2.27)$$

$$\frac{H_x^{n+1}(i,k+1/2) - D_y^n(i,k+1/2)}{\Delta t} = -\frac{1}{\sqrt{\varepsilon_0 \mu_0}} [(\frac{E_y^{n+1/2}(i,k+1) - E_x^{n+1/2}(i,k)}{\Delta z}) \qquad (2\text{-}2.28)$$

$$\frac{H_z^{n+1}(i+1/2,k) - H_z^n(i+1/2,k)}{\Delta t} = \frac{1}{\sqrt{\varepsilon_0 \mu_0}} [(\frac{E_y^{n+1/2}(i+1,k) - E_x^{n+1/2}(i,k)}{\Delta x}) \qquad (2\text{-}2.29)$$

The functions above are similar to that mentioned in the 1-D FDTD method.

2-3 Coupling mechanism

Coupling mechanism is important for many applications in optical communication and integrated optics. A simplest form is a directional coupler consists of two parallel waveguides. If two waveguides are close enough such that their field will overlap, and the light will couple from one waveguide to the other one. Optical power could be transferred between two waveguides hence it is used to make optical switches and couplers. As shown is fig 2-3.1 the n_1 and n_2 are the refractive index of the materials embedded in the material with refractive index is n, and the both two waveguides are single mode.
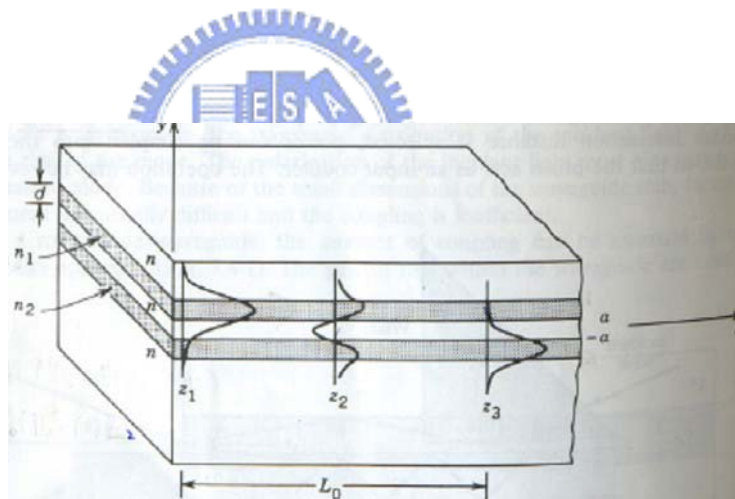

Fig. 2-3.1 The coupling mechanism between two parallel waveguides. When light is injected at z_1 the field is almost in the waveguide 1. At z_2 the light is equally divided in two waveguides, and at z_3 the field is almost transferred from waveguide 1(w_1) to waveguide 2(w_2).

For a simple representation, a combined structure of the two waveguide supports an even and a odd modes, and the action of a coupler could be explained as follows. At the input, the directional coupler is excited with a field, and this initial field could be expressed as the sum or difference of the even and odd modes of the

combined structure. In 2-D FDTD simulation, the EM wave could transfer from the first channel to the second channel as show in Fig. 2.3-2
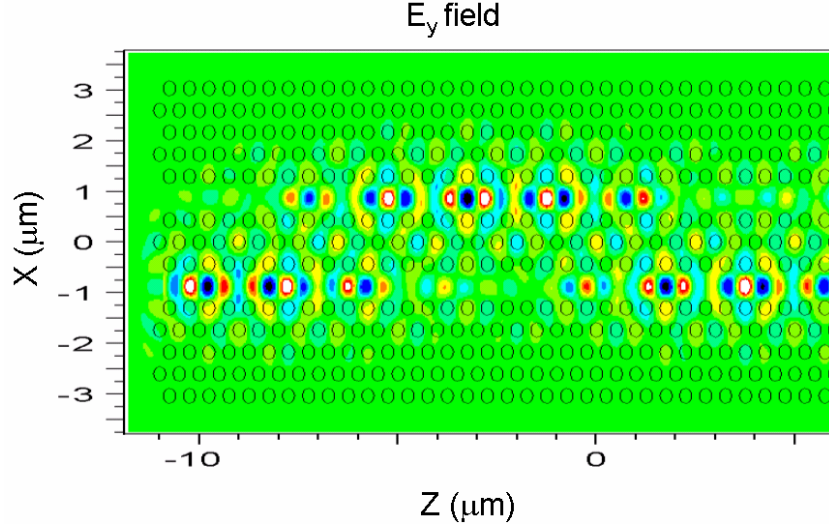

Fig. 2.3-2 The E_y field in a planar PC waveguide with two channels calculated by "FullWave" software.

In Ref. [20], if there is no interaction between the two waveguides, a normal mode of one isolated waveguide is also a normal mode of the system of the two waveguides. Let us symbol the mode localized in the first waveguide as $|\psi_1\rangle$ and that in the second waveguide as $|\psi_2\rangle$. These two modes have the same frequency ω. They are degenerate (twofold) states. Once a perturbation is switched on, this frequency splits into two frequencies ω_1 and ω_2, where $\Delta\omega = \omega_1 - \omega_2 << \omega$. Here we exactly distinguish the normal modes $|\psi_1'\rangle$ and $|\psi_2'\rangle$ of the perturbed system corresponding to these frequency. And the function in the first waveguide, we could write as

$$|\psi_1\rangle = C_1|\psi_1'\rangle + C_2|\psi_2'\rangle \tag{2-3.1}$$

For a time evolution of the EM wave, Eq. (2-3.1) could be written as

$$|\psi_1\rangle = C_1|\psi_1'\rangle e^{i\omega_1 t} + C_2|\psi_2'\rangle e^{i\omega 2t} \tag{2-3.2}$$

If the two waveguides are identical, $|C_1| = |C_2|$. And the Eq. (2-3.2) can be simplified as

$$|\psi_1\rangle = \phi(r) \cdot \sin(\frac{\Delta\omega}{2} \cdot t) \cdot \sin(\omega \cdot t) \qquad (2\text{-}3.3)$$

From Eq. (2.2-3), we can see that the time T of the transformation of state $|\psi_1\rangle$ to $|\psi_2\rangle$ is $0.5 \cdot (\Delta\omega/\omega) \cdot T_0$, where T_0 is the period of the EM field oscillation. The value of the frequency splitting $\Delta\omega$ due to the interaction between be evaluated by MIT photonic-bands simulation (Plan Wave Expansion) using the super cell approach, the super cell includes the two interactive waveguide. Now we start to evaluate the coupling length:

$$L = T \cdot v_g \qquad (2\text{-}3.4)$$

In the equation above, the group velocity, $v_g = d\omega/dk$, can be obtained form the MPB band structure calculation. Substituting the following Eq. (2-3.5) and $v_g = d\omega/dk$ into (2-3.4)

$$T = 0.5 \frac{\omega}{\Delta\omega} T_0, \qquad (2\text{-}3.5)$$

finally we can determine the desired coupling length which has the form

$$L = 0.5 \frac{\omega}{\Delta\omega} v_g T_0. \qquad (2\text{-}3.6)$$

And then if we replace the v_g by $d\omega/dk$ and T_0 by $\frac{1}{f}$ (where T_0 and f are

normalized wavelength and frequency) in Eq. (2.5-5). The coupling can be expressed by using the split normalized wave-vector (Δk) bellow.

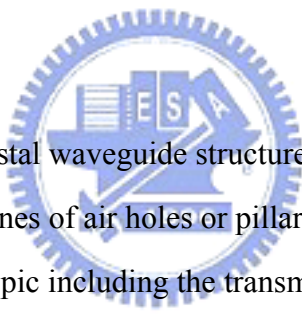$$L = \frac{\pi}{\Delta k}$$

(2-3.7)

Equation (2-3.7) is often used to calculate the coupling length.

Chapter 3 Simulation results

Here we will discuss some researches in 2-D photonic crystal waveguide and applications. Three subjects are shown, including line-defect PCs waveguide, Y-type power splitter, and coupling/decoupling wavelength selected switch. The PWE method is used to calculate the band diagram; the FDTD is used in power transmission.

3-1 Single line-defect PC waveguide

A basic photonic crystal waveguide structure is a line-defect waveguide, which is removed one or more lines of air holes or pillars in the photonic crystal. There are many researches in this topic including the transmission, absorbency, group velocity, etc. in both simulation and measurement areas. Here some discussions will be shown below Fig. 3-1.1. Commonly speaking, the square lattice structure with the dielectric rods is used to transfer the TE mode, and the triangular lattice structure with the air holes is used to transfer the TM mode. It's clear to see that the band diagrams have shown the transmissions of all kind structures. The simulations are calculated by the "FullWave" software. Most researches have shown the power transmission is related to the band diagram. In the band diagram the defect mode could be divided to two parts, one is the linear region, and the other is the band-edge region. When the wavelength is in the linear region we could get high power transmission, but it is in the band-edge region the power transmission drops sharply.
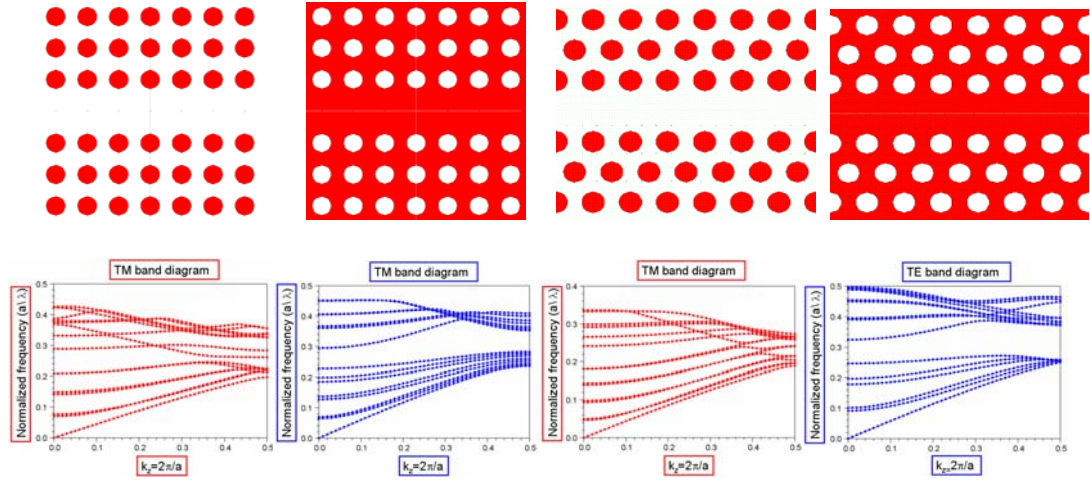
Fig. 3-1.1 The single-line defect photonic crystal waveguide with r/a ratio is 0.3.

Here, the white is the dielectric material (n = 2.8), and the red is the air (n = 1). (a) Square lattice with dielectric materials. (b) Square lattice with air holes. (c) Triangular lattice with dielectric materials. (d) Triangular lattice with air holes.

Now we increase the width of the channel, and the width is increased by the step of 75nm (the PC device parameter is set r/a = 0.3 and n = 2.8). To calculate the band diagram by using the Plane Wave Expansion method, and we compare to the normal single line defect.

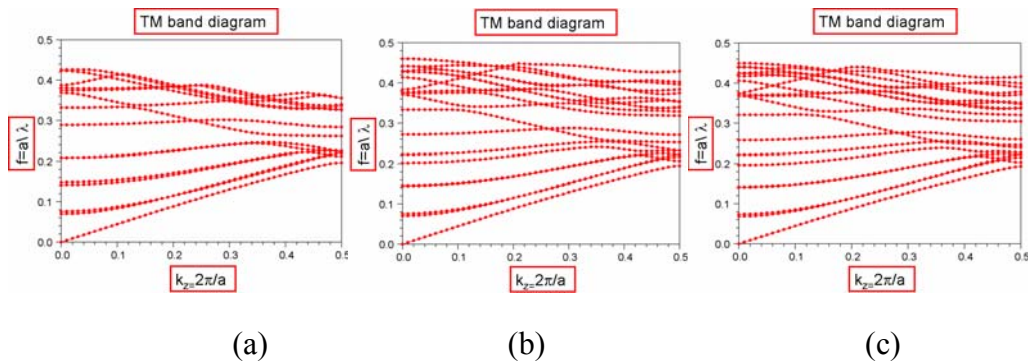(a)   (b)   (c)

Fig 3-1.2 The band diagram graphs of the different width structure. (a) The normal structure. (b) The width is increased 75nm (c) The width is increased 150 nm.

We could see the band gap in Fig. 3.1-2c is smaller than that in Fig. 3.1-2a, and the defect modes in the gap increase. Hence, the power transmission versus the

wavelength is shown below. In the band diagram, the larger width has the more modes in the high frequency.
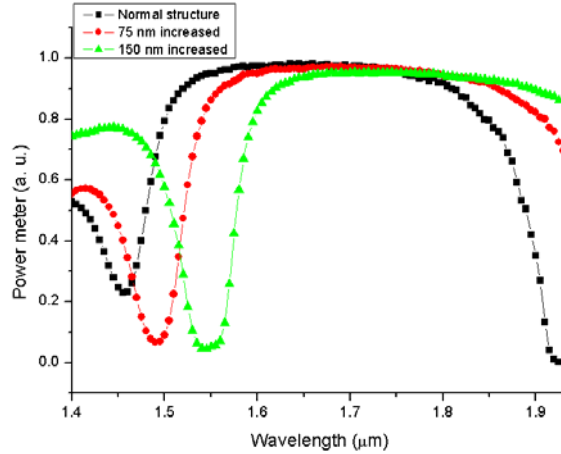

Fig. 3-1.3 The power transmission of the waveguides with different width.

In the simulation we put the time monitor in the PC waveguide, but in the real case our detector is out of our device. Hence the location in the PC waveguide could tell us that the characteristic of the PC waveguide device, but if we want to use it to compare to our measurement data, the power meter of the simulation has to change its' location. In the real case the power meter is set in the free space (n = 1), therefore the condition of the simulation is changed and show in Fig. 3-1.4.
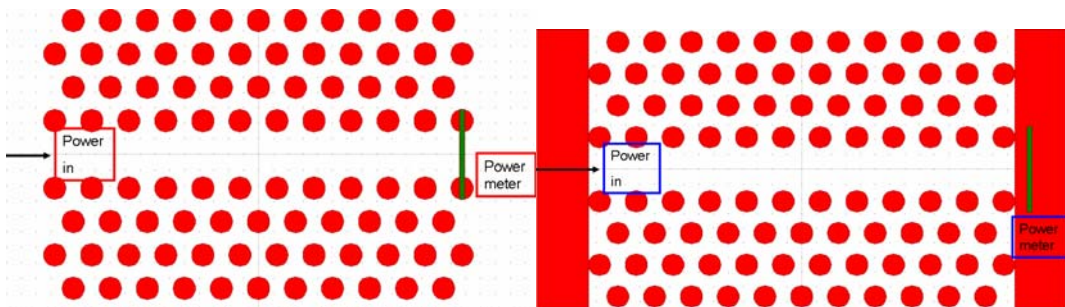

Fig. 3-1.4 The schemes of the different locations of the power meters. (a) The power meter in the device. (b) The power meter in the free space. The red and white colors represent the air and dielectric region.

If the power meter is set in the free space, the Fabry-Perot effect will happen like the conventional waveguide.

$$\frac{I_{out}}{I_{in}} = \frac{1}{1 + F \cdot Sin^2(\frac{\delta}{2})} \tag{3-1.1}$$

$$F = (\frac{2r}{1+r^2}) \qquad \delta = \frac{2\pi d}{\lambda} \tag{3-1.2}$$

$$r_\perp = \frac{n_i \cos\theta_i - n_t \cos\theta_t}{n_i \cos\theta_i + n_t \cos\theta_t} \tag{3-1.3}$$

Here, the F is the **Finesse Coefficient,** r is the **amplitude reflection coefficient,** n_i, n_t is the refractive index of the dielectric material and free space, and λ is the wavelength in the dielectric material. Therefore, the out power will have the interference in the different wavelength.
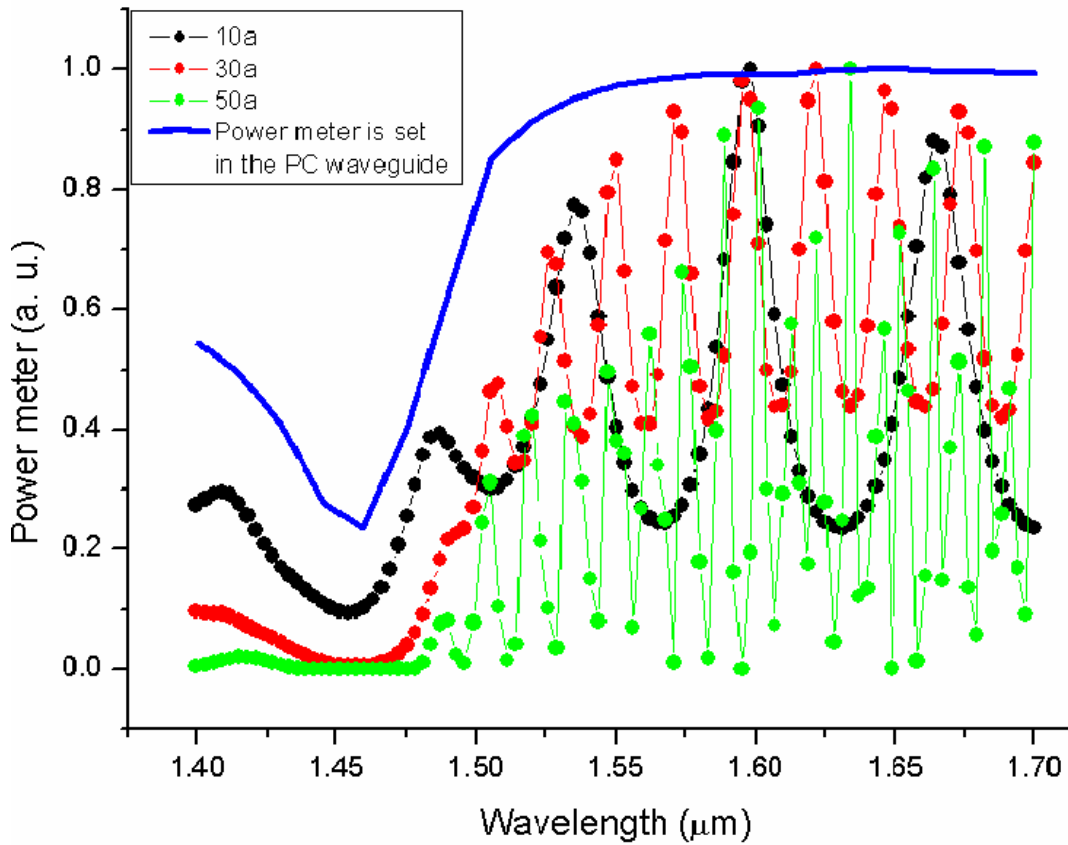

Fig. 3-1.5 Power transmission (with resolution is 3 nm) of different length of the PC waveguide (r/a = 0.3) with the power meter located in the air except the blue line is set in the PC waveguide to show the characteristic of this device

3-2 Coupling-type PC power splitter

3-2.1 Introduction

Over the past two decades, the potential of photonic crystals for different applications has been discussed intensively [3,21]. Photonic crystal devices are very suitable for photonic integrated circuits due to the minimization of the device dimensions. In recent years, nano-meter fabrication technology becomes more and more mature. As a result, many photonic crystal devices have been realized, such as photonic crystal waveguide multiplexers/demultiplexers on a two-dimensional (2D) photonic crystal slab. Power splitter is one of the important devices for future realization of photonic integrated circuits. Here we design a new type of power splitter using the concept of coupled mode theory on 2D photonic crystal waveguides (PCWGs) [29] with hetero-structures [30]. This new design has the characteristics of high power transmission and short coupling length. Furthermore, the structure proposed solves the low extinction ratio caused by short coupling length [32]. In this report, a power-splitter device for 1550nm with an ultra-short coupling length about 9.3μm and a high coupling efficiency above 90% is presented utilizing the hetero-structure in PCWGs.

3-2.2 Structure design and simulation

First, basic coupling-type photonic crystal power splitters are considered with three rows of air holes removed from a triangular photonic crystal lattice as shown in Fig. 3-2.1(a) [32]. The middle input channel is labeled port 1 and the other two

output channels are labeled port 2 and port 3. The separation between two adjacent channels is three rows of air holes.   The photonic crystal lattice with uniform r/a ratio 0.3 is used, where r is the radius of air hole and a=423 nm is the lattice constant. Fig. 3-2.1 (b) shows the band diagram of the basic structure introduced in Fig. 3-2.1 (a), and the coupling mechanism is utilized to transfer the power of the middle input channel to the other two output channels. The forward continuous wave (CW) signal is injected to port 1 from the left side and couples to the other two channels equally as it propagates.
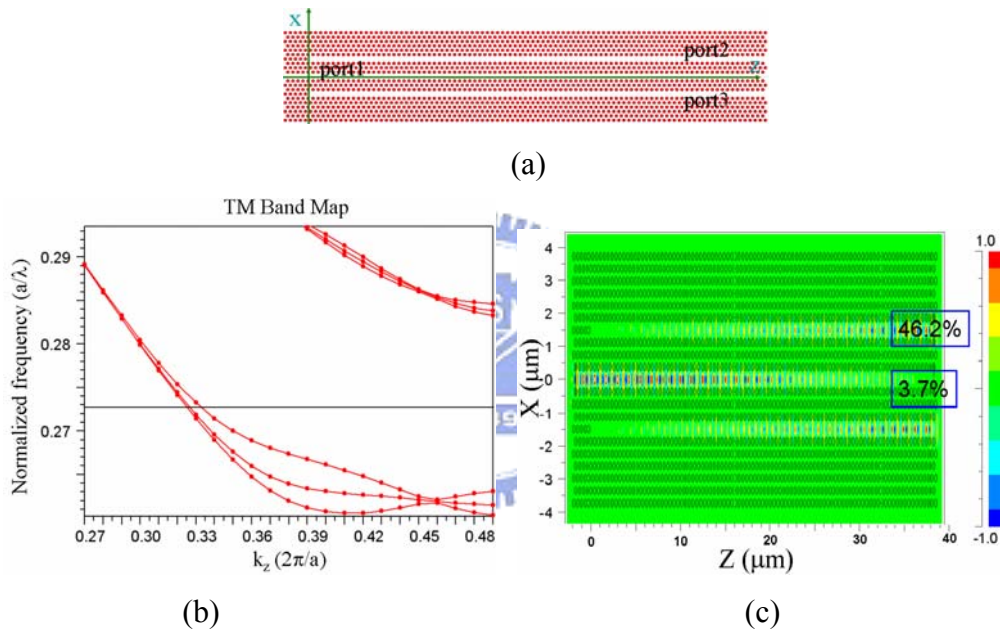

(a)

(b)

(c)

Fig. 3-2.1: (a) Basic coupling-type photonic crystal power splitter with uniform r/a ratio 0.3. (b) Its band diagram. The green, blue, and red lines label the 0th, 1st, and 2nd defect modes. The olive solid line indicates the normalized frequency 0.2728. (c) Power flow plot when $\lambda=1.55\mu m$.

For the structure shown in Fig. 3-2.1 (a), there are three defect modes existed which are labeled 0th, 1st, and 2nd [31] modes, respectively, and are indicated by green, blue, and red lines in Fig. 3-2.1 (b). Their corresponding mode profiles are shown in Fig. 3-2.2 (a), (b), and (c). Since we focus on communication applications,

the wavelength chosen in our design is 1550nm, which corresponds to 0.2728 in normalized frequency and is indicated by the solid olive line in Fig. 1 (b). However, only 0th and 2nd modes can be excited because 1st mode is odd-symmetry with respect to the propagation axis (z-axis). Therefore, two even-symmetry modes are taken into account for the calculation of coupling length L. The total field f can be expressed as a superposition of 0th and 2nd mode fields f_0 and f_2 as in Eq. (3-2.1), where A_m is the field excitation coefficient and k_m is the propagation constant of the mth mode.

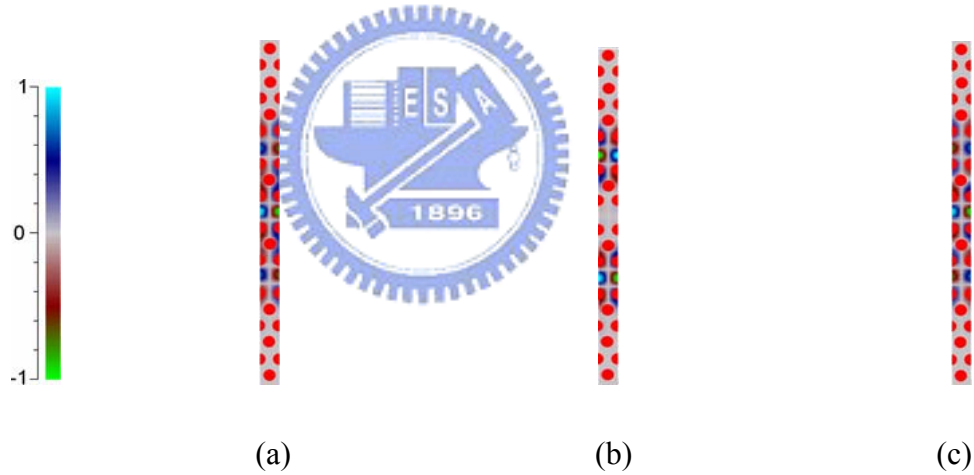$$f(x,z) = A_0 f_0(x,z)e^{-jk_0 z} + A_2 f_2(x,z)e^{-jk_2 z} \tag{3-2.1}$$

| | (a) | (b) | (c) |

Fig. 3-2.2: Mode profiles of H_y in a unit cell for (a) 0th, (b) 1st, and (c) 2nd modes for the structure shown in Fig. 1 (a) with r = 0.3a. The amplitude scale is on the left side; the red circles represent air holes.

After propagating a distance equal to the coupling length ($z=L$), the wavefunction $f(x,L)$ will satisfy the coupling condition:

$$\begin{aligned} f(x,L) &= A_0 f_0(x,L)e^{-jk_0 L} + A_2 f_2(x,L)e^{-jk_2 L} \\ &= \left[A_0 f_0(x,L) - A_2 f_2(x,L) \right]e^{-jk_0 L} \end{aligned} \tag{3-2.2}$$

From Eq. (3-2.2), the coupling length L can be defined as (n is zero or positive integer)

$$L = \frac{(2n+1)\pi}{|k_2 - k_0|} \qquad (3\text{-}2.3)$$

When the wave propagates a specific length (coupling length), the phase shift is equal to π (n=0) and energy transports to other channels by changing of 0th and 2nd modes. The difference of the two propagation constants k_2 and k_0 can be found from the band diagram shown in Fig. 1 (b). Therefore for a field at 1550nm, the coupling length for the structure with r=0.3a is 90a. Power flow inside this structure at 1550nm is shown in Fig. 3-2.1 (c). Total power transmission of port 2 and port 3 combined is 92.4%, and the extinction ratio is 14dB. Here the InP/InGaAsP material system is assumed, and 2D finite-difference time-domain (FDTD) method is used with an effective refractive index 2.8. In this case, the coupling length is about 38.1μm. This is too long for the design of dense photonic integrated circuits. To obtain a shorter coupling length, we consider the structure with 0.33r/a ratio as shown in Fig. 3 (a). Its band diagram is shown in Fig. 3-2.3 (b) and power flow inside this structure at 1550nm is shown in Fig. 3-2.3 (c). The coupling length for r/a=0.33 is only 12a, which is about 5.1μm, but total power transmission in port 2 and port 3 is only 75.2% and the extinction ratio is only 6.7dB. Considering the coupling properties with respect to the coupling length, it has been clearly shown that the power will not transfer from one channel to another completely in a short coupling length [33].

(a)

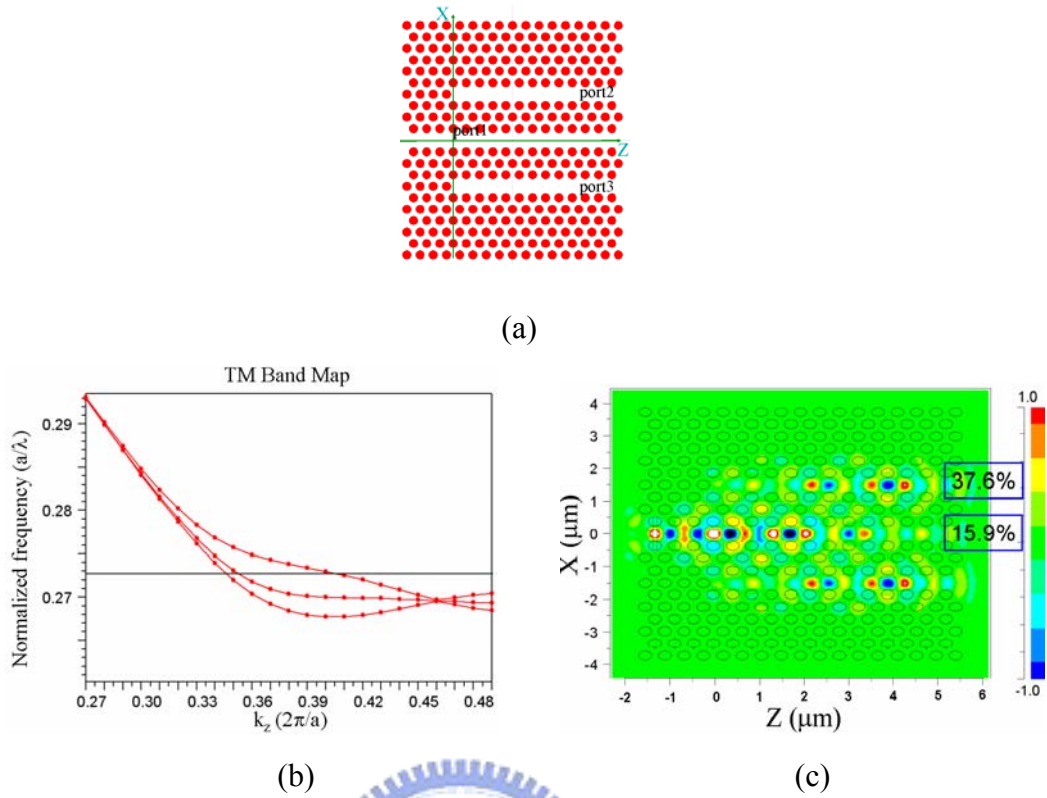(b)   (c)

Fig. 3.2-3: (a) Basic coupling-type photonic crystal power splitter with uniform r/a ratio 0.33. (b) Its band diagram. The green, blue, and red lines label the 0th, 1st, and 2nd defect modes. The olive solid line indicates the normalized frequency 0.2728. (c) Power flow plot when λ=1.55μm.
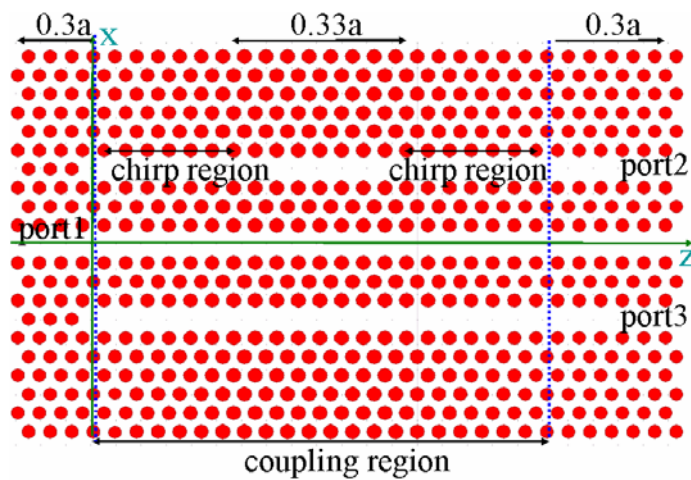

Fig. 3-2.4: Coupling-type power splitter with hetero-structure photonic crystals.

The characteristics of basic coupling-type photonic crystal power splitters can not meet our needs for high power transmission with short coupling length at the same time. In order to solve this problem, we design a new coupling-type power splitter with hetero-structure PCWGs as shown in Fig. 3-2.4 to improve the extinction ratio and decrease the coupling length.   The radius of all air holes is 0.3a at the input and output regions of the PCWGs, but at the coupling region the radius is changed from 0.3a to 0.33a by a step of 0.005a and then back to 0.3a by a step of 0.005a too as shown in Fig. 3-2.4. The air hole radius variation can be expressed as:

$$r(z) = \begin{cases} 0.3a & (0 \le z < a) \\ 0.005z + 0.295a & (a \le z < 7a) \\ 0.33a & (7a \le z < 15a) \\ 0.33a - 0.005(z - 15a) & (15a \le z < 21a) \\ 0.3a & (21 \le z < 22a) \end{cases} \quad (3\text{-}2.4)$$

Again we can calculate the band diagrams for different r/a ratios and then the differences $\Delta k(z)$ of the two propagation constants (k_2 and k_0) at f = 0.2728(a/λ) can be obtained from band diagrams and fitted as a second-order polynomial function that varies with z in the chirp region.

$$\Delta k(z) = 0.0015z^2 - 0.0068z + 0.0129 \quad (\frac{2\pi}{a}) \qquad (3\text{-}2.5)$$

To fully transfer the field, the phase difference should equal *(2n+1)π* when the wave propagates a distance *L*.

$$(2n+1)\pi = \int_0^L \Delta k(z)dz \qquad (3\text{-}2.6)$$

Using our design, the phase difference after propagating *L=22a* distance calculated using the right-hand side of Eq. (3-2.6) is about *1.05π*, which is very close to π (*n=0*). The small difference can be resulted from the approximation occurred when fitting the polynomial. Therefore, the coupling length for the proposed hetero-structure photonic crystal power splitter is about 9.3μm according to coupled mode theory.


(a)
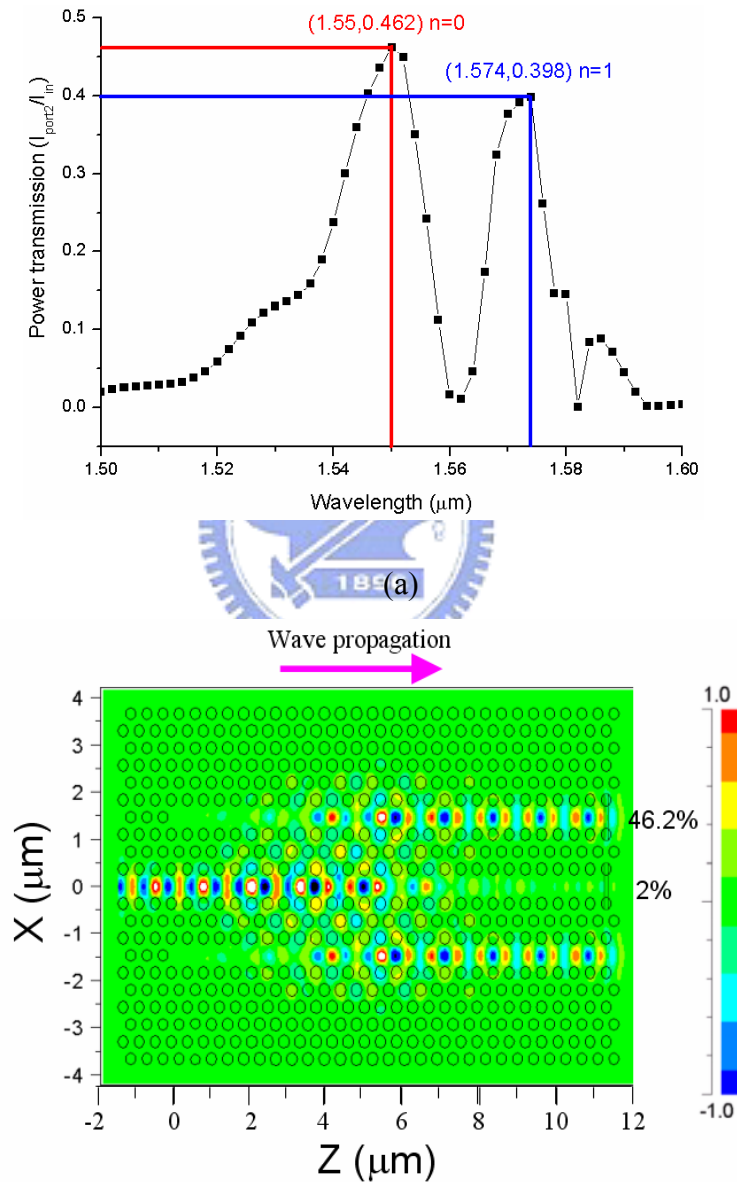
(b) Fig. 3-3.4:

Fig. 3-2.5 (a) Power transmission versus normalized frequency for coupling-type power splitter with hetero-structure photonic crystals. (b) Power flow plot when λ=1.55μm.

We also use 2D FDTD method to calculate power transmission versus normalized frequency at port 2 for the proposed hetero-structure photonic crystal power splitter. The result is shown in Fig. 3-2.5 (a). We can clearly see that power transmission is peaked at normalized frequency 0.2728, which means that our proposed structure is optimized for wavelength at 1.55μm with high power transmission. This result also agrees with the one obtained using couple more theory. Power flow inside this structure at 1550nm is shown in Fig. 3-2.5 (b). Total power transmission for port 2 and port 3 combined is 93.4% and the extinction ratio is 16.7dB. Hence, using the proposed hetero-structure photonic crystal power splitter, short coupling length and large extinction ratio can be obtained simultaneously. Here, when the wavelength is 1574 nm in Fig. 3-3.5 (a), the power will translate from channel 1 to channel 2 and 3 and back to channel 1 and then go to channel 2 and 3 again. Furthermore, if we choose a suitable condition, the triple-lines channel with equally power transmission will be created, here the wavelength is 1542.5 nm.
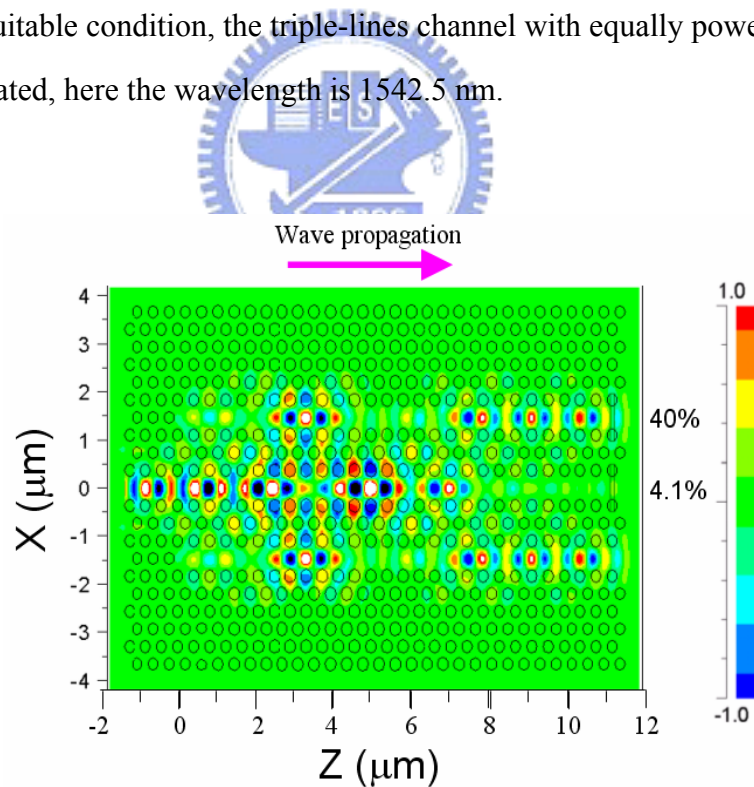
(a)
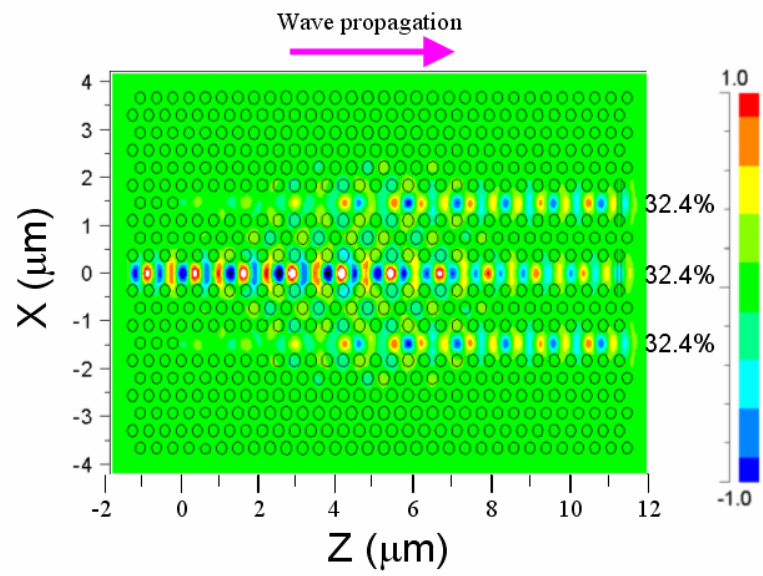
(b)

Fig. 3-3.5 (a) The wave propagation with $\lambda = 1574$ nm (n = 1) (b) The power is equal

in all channel with $\lambda = 1542.5$ nm.

Chapter 4 Fabrication and measurement of PC waveguides

To fabricate the photonic crystal waveguide, we used the PECVD to deposit $1400 \dot{A}$ SiN on InGaAsP wafer and the E-Beam Lithography System is used to do the next process. Before E-beam lithography, the PMMA was spin coating on the SiN about $3000 \dot{A}$, and then the pattern drawn by Auto-cad software was lithographed by the E-beam system. The following step we used Inductively-coupled plasma etching system (ICP) to etch the SiN; the pattern was transferred to the SiN, soon we removed the PMMA by ICP again. After the pattern was transformed to the SiN, we increased the temperature the chamber for dry etching and removing the hard mask, SiN. When the E-beam lithography and dry-etching processes were finished, the undercut process was the next step for our membrane structure. In this process, we use specific acid solution to erode the InP material but won't erode the InGaAsP material in order to construct the photonic crystal waveguide with the membrane structure. After undercutting the device, we use a machine (Karl-SUSS 120) to scribe upon our samples. A diamond-tipped scribe was scored across the wafer creating lines on the wafer surface. And then the wafer was stressed, the wafer separates along the scribed lines. Final, we could get our photonic crystal waveguides membrane samples.

4-1 Fabrication process

In the first step the SiN layer with the thickness $1400 \dot{A}$ is deposited on the InP cap layer by Plasma Enhanced Chemical Vapor Deposition (PECVD) system with the gaseous mixture of $SiH_4/NH_3/N_2$. The thickness of SiN layer is chosen to sustain

the deep etching of InGaAsP/InP layer later, which is take into account the InP/SiN etch selectivity and allowing for an etch lag in deep holes.

The cad files are important for fabrication process, so we discuss the design about our cad file first. In our cad files, the length of photonic crystal is about 300 μm, and at the two terminations of the photonic crystal waveguide there are two big windows 30 μm x 13 μm, they are designed to be scribing on them. We want the broken plane through these two big windows to avoid destroying our photonic crystal waveguide device. In the lateral sides of the photonic crystal waveguide, there are many small windows, 5 μm x 5 μm, which are crisscrossing to each other. They can let acid solution permeate the host InP and undercut sample more easily. The cad file design is shown in Fig. 4-1.2, and the size of these windows is very important to etching and splitting of the sample.
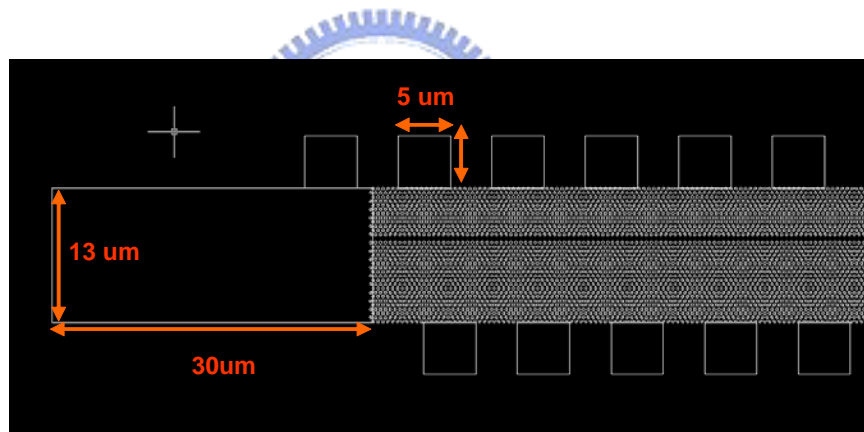

Fig. 4-1.2 The cad file of photonic crystal design.

Then the positive resist PMMA (3000 $\mathring{A}$) (A5) is used to spin coating on the wafer with the suitable size, and the defined pattern is transferred on PMMA by E-beam lithography system. After E-beam defined pattern, we use MIBK to clean the positive resist. And the channel of our photonic crystal waveguide will be along <0,-1,-1> direction. But the total length of the limitation of our E-beam lithography system is about 300 μm. The top view of the photonic crystal waveguide with 300 μm is shown In Fig. 4-1.3.
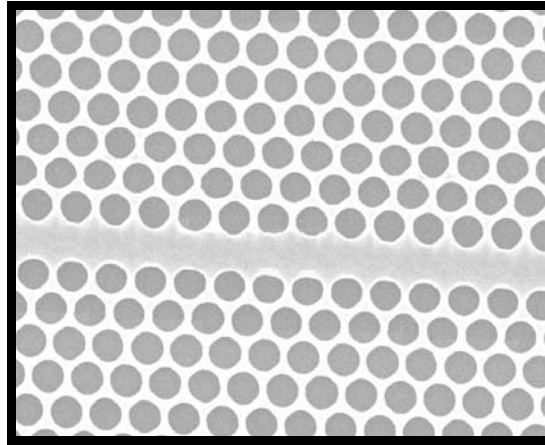
Fig. 4-1.3 Defined pattern 300um length on PMMA and writing magnification
is ~ 300 x

After we successfully define pattern on PMMA by E-beam lithography system, we
transfer the pattern to SiN by using the Inductively-coupled plasma etching system
(ICP). Then we remove the PMMA by O_2 plasma etching and clean the chamber
5min. Furthermore in order to etch the InGaAsP layer, we first have to warm up the
temperature of the chamber to 150 degree and use mixture gases $H_2/Cl_2/CH_4$.
In our structure we want to etch cap layer 60nm and InGaAsP 250nm, hence the
depth of 300nm must be achieved; the etching time is 105 seconds to etch into host
InP in our design structure. The last step to fabricate the membrane photonic crystal
waveguide is to undercut the waveguide. We first glue to the sample on a glass by
PMMA instead of clipping the sample, it's because the stress of clipping may break
the sample. Then we use the acid solution (HCL : H_2O =3:1), the recipes of time and
temperature are 80 minutes and 3^0C, to erode the host InP and the cap layer but not
InGaAsP. The wet etching case two etch stop plane for InP etching, the two
directions are 40° in <0, 1, -1> direction, 95 ° in <0, -1, -1> direction. Then along
<0,-1,-1> direction the bottom of waveguide would be penetrated, and the membrane
structure is formed. Here, for examples, if the cad file is not well design, the
waveguide would collapse shown in Fig. 4-1.5(b). Fig. 4-1.5(a) is the top view of
waveguide broken by wrong cad design for connection of photonic crystal
waveguide and ridge waveguide. Fig. 4-1.5(b) is the SEM of broken waveguide by a

tilted angle. So the cad file is very important to design. The second, the time of the wet etching process is very important, too, if the time is not enough, the InP substrate will not be penetrated
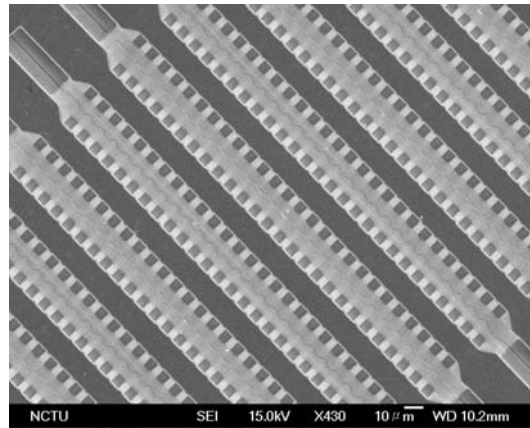

Fig. 4-1.4 The SEM figure of successful undercut sample which soaked time is 80mins.
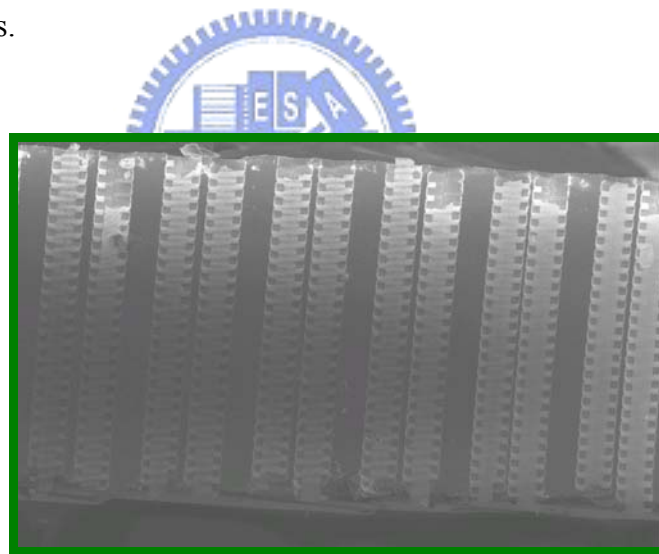

Fig. 4-1.5 The device we have cut the wafer.

After undercutting the wafer, we use the wafer scribe (Karl-SUSS 120) to cut samples. A diamond-tipped scribe is dragged across a wafer creating a scratch in the wafer surface. When the wafer is stressed, the wafer separates along the scribe lines, the Fig. 4-1.9(a) is the concept after diamond-tipped scribe is dragged across a wafer. The breaks follow the crystal structure of the wafer, creating a right-angle edge direction. Finally we get photonic crystal waveguides membrane samples. The Fig. 4-1.9(b) is the device we have cut the wafer.

4-2 Measurement of the photonic crystal waveguide

The experimental setup for observing the transmission spectrum of a PC waveguide is constructed. In order to identify a particular spectral region in the transmission spectrum with that specific to the simulation, we observed the spectrum over a wavelength region from 1470 to 1510 nm by using a spectroscopic method suited for a sample with very thin and small input-facet like the present one. The schematic is shown in Fig. 4-2.1.
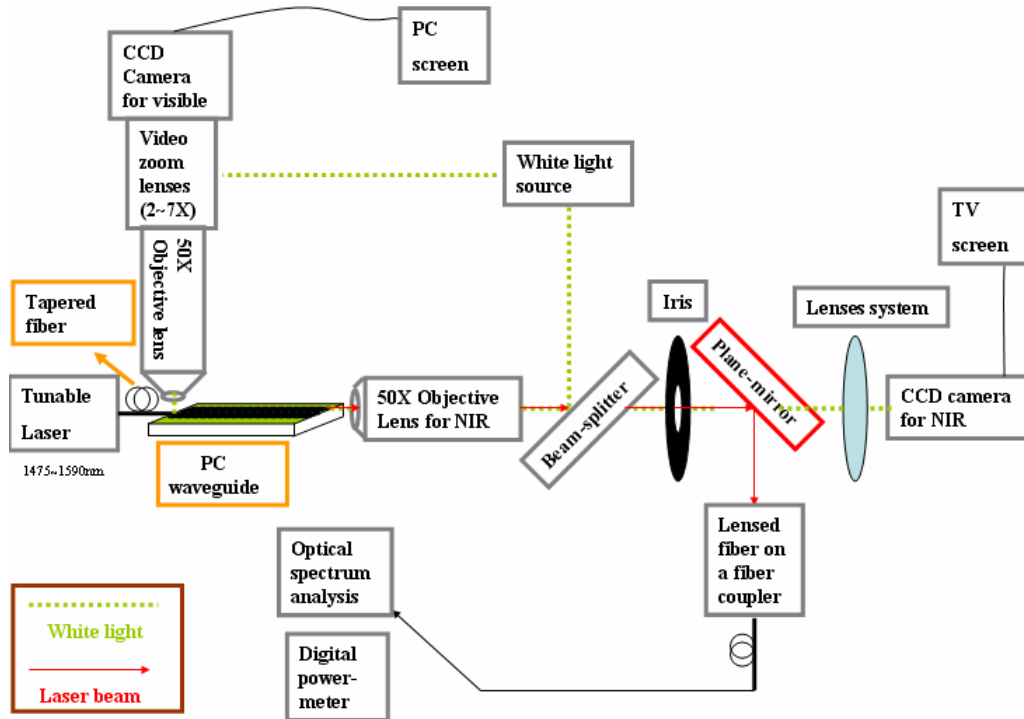

Fig. 4-2.1 The schematic of the microscopic system for the top and back views of the PC waveguide device.

Two commercially-available white-light are used as the present sources (the olive lines). The input light is connected to the tunable laser (Hp 8168) through a FC connector by a polarization maintained tapered fiber (which is shaped to be a lens by polishing) for single mode. The output light is focus by the tapered fiber, and its' diameter of the spot about 2~2.5 μm. Then, output light from the fiber was focused

onto the cleaved input-facet of the PC waveguide, and the signal appearing at the output-facet was picked up by another lensed fiber. The signal light was introduced to the optical spectrum analysis (OSA, Ando AQ-6315A) having the sensitivity from 350~1750nm. The tapered fiber and the sample are set on the six axes stage respectively, and both of these two stages are on a one-axis big plate.

In the camera view, the back view, for the optical coupling between the tapered fiber and the PC waveguide, shown in the Fig. 4.2-2 is obtained by a 50X objective lens for NIR region, convex lenses system, and a CCD camera (7260A) which is suitable for the NIR region. The top view, for the alignment between the fiber and the device, is observed by a 50X objective lens, a video zoom lenses system, and a CCD camera (CC-560) for visible light region. And the top view (Fig. 4.2-3a) and back view (Fig. 4.2-3b) are connected to the computer and the TV respectively.
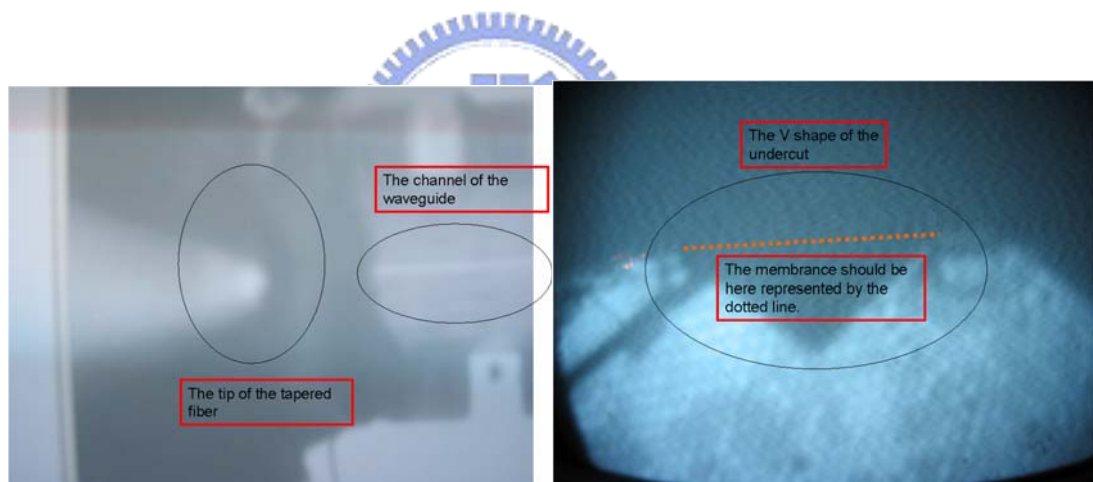

Fig. 4-2.3 (a) The top view of the microscopic system. (b) The back view of the microscopic system.

In the measurement process shown in Fig. 4-2.4, the coupling between the optical fiber and the PC waveguides is very important. If the fiber doesn't couple well, the transmission will low or the noise will high. In the process of fine coupling, we use the light source of the tunable laser with the wavelength is 1550 nm (6mW), it's because the max power of the tunable laser is not the same versus the wavelength.
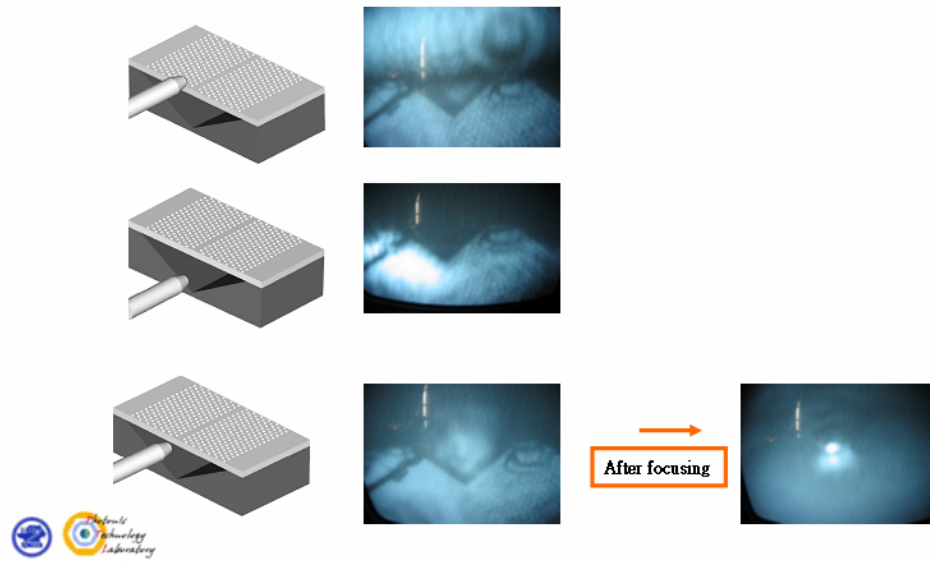
How to measure the signal

After focusing

Fig. 4-2.4 The processes of the PC waveguide measurement.

In Fig. 4-2.5(a) the fiber is higher than the channel, and in Fig. 4-2.5(b) the fiber is below the channel. Both two cases will bring the high noise. In the left graph of the Fig. 4-2.5, most power is scattering upper the PC device, and the single passes the waveguide is small. In the right graph, most power is transmission from the InP substrate (refractive index is 3, so the InP could also be a large waveguide if the power is high enough.).

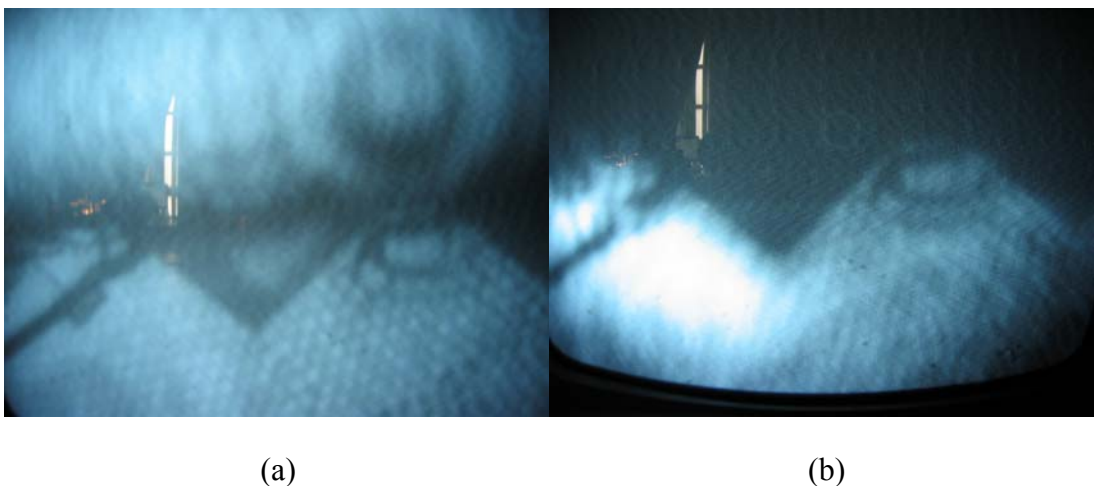(a)   (b)

Fig. 4-2.5 (a) the spot is focused by the fiber upper the waveguide, and the light is scattered from the top of the device. (b) the spot is focused down, the power will transfer by the InP substrate.

Hence, the back view is important to recognize if the coupling is good, and the top view is used to distinguish which one PC waveguide couples to the fiber. When the fiber is well alignment to the channel we will see a spot when we move the one-axis stage to focus the image shown in Fig. 4-2.4.

And in order to make sure the fiber and the channel are well coupling, we use some processes. First, the tip of the tapered fiber is put in the photonic crystal region (the left or right side of the channel), and move it up and down. If the fiber is upper or down the membrance device, Fig. 4.2-4 have shown the cases. Therefore, if the fiber is aligned well, we can not see any light in the video (this is a ideal case, and there is still a little amount light scatters). When the scattering light is small enough, we could make sure that the fiber is focused in the membrance, then to remove the fiber to the channel.

To measure the power transmission is another issue. The measurement setup has shown previously in Fig. 4-2.1. The output power is focused by the 50X objective lens and reflected by a planar mirror to a 20X objective lens to focus on the lensed fiber; here, the planar mirror and lensed fiber are set on the fiber coupler stage. In the beginning we didn't add the iris between the beam-splitter and planar mirror; hence we got the noise. The noise affected the received single a lot. Finally, we added the iris into the system to block the signal transferring from the free space or the InP substrate.
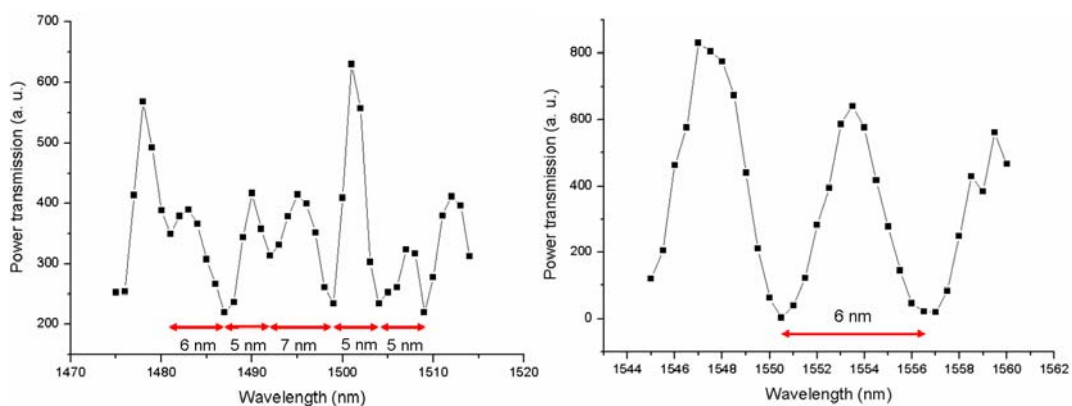

Fig. 4-2.6 The measurement data in different wavelength region (a) 1475~1515 nm with step of 1nm. (b) 1545~1560nm with step of 0.5 nm.

In Fig. 4-2.6, the measurement data has shown, I measured the device in different time within different wavelength regions, and both tell us the device has the Fabry-Perot effect which also has the period about 6 nm. And then we check the length of the PC waveguide by the function below:

$$L = \frac{\lambda^2}{2n_{eff} \cdot d\lambda \cdot Cos\theta}$$

(4-2.1)

, the length is 78.9 μm. In Eq. (4-2.1), λ is 1554 nm, the n_{eff} is 2.8, and $d\lambda$ is a averaged value with 5.5 nm. This result is not accuracy to our device shown in Fig. 4-2.7. The reason is the optical device like objective lens dominates the Fabry-Perot effect. Hence how to decrease the effect caused by optical device is an important issue.
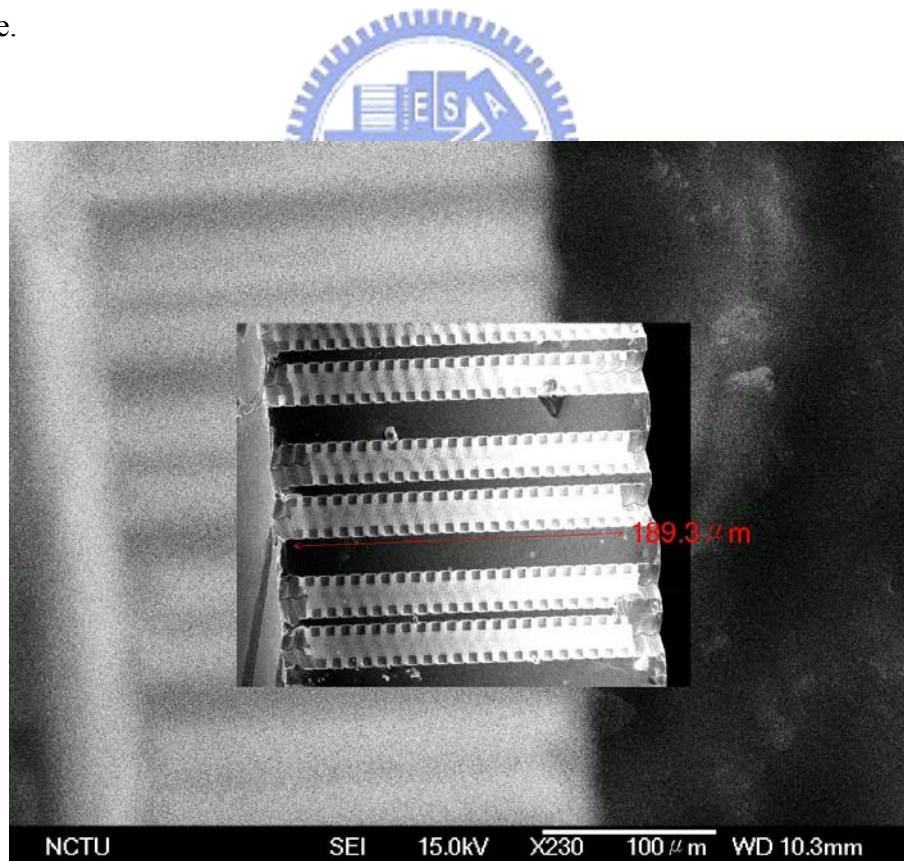

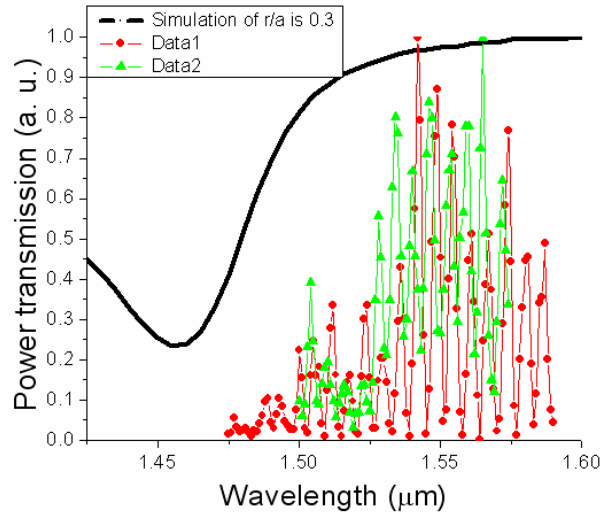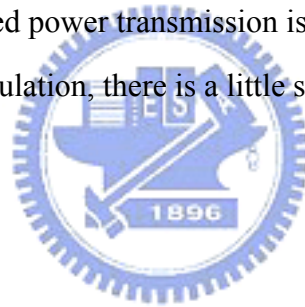Fig 4-2.7 The PC waveguide device

Fig. 4-2.8 The graph of the simulation and measurement of single line defect

waveguide

In Fig. 4-2.8, the measured power transmission is low before 1500 nm and increases

after 1525 nm. In the simulation, there is a little shift, but the tendency is match to

the measure data.

Chapter 5 Conclusion

In this thesis, a hetero-structure photonic crystal coupling-type power splitter with an ultra-small size, only 9.3μm long, and a high power transmission above 90% is presented. Our design solves the low coupling efficiency problem caused by short coupling length and offers a high extinction ratio. Furthermore, we do not have to fine tune the lattice structures for high power transmission, which is needed in Y-splitters due to the impedance mismatch [28]. This device is very useful in photonic integrated circuits due to its small dimension. If high-transmission photonic crystal waveguide bends, for example, with planar mirrors (the design of my partner ',Shu-Jhih Chen), are combined with hetero-structure photonic crystal coupling-type power splitters, a multi-port power splitter can be constructed and ultra-dense photonic integrated circuits can be realized. Although our design is not a broad band device, but it's worth for specific wavelength as WDM system. And in special conditions the power will all the same in each channel with phase shift. This phenomenon could be used in Mach-Zander interference.

In the processes of PC waveguide, the big problem is in cutting the device. Before this step, we have successfully made our sample. It's because the device is too small, hence we have to polish it before cutting it. This will cause the sample thin and brash. The yield for the manufacture of our device is low. About our measurement setup, I think it's well enough for PC waveguide measure. The output spot focused well is clear; it's will miss when we move the device. I think the our setup could measure the signal of the PC waveguide.

References

[1] E. Yablonovitch, "Inhibited Spontaneous Emission in Solid-State Physics and Electronics," Phys. Rev. Lett. 58, 2059-2062, 1987

[2] S. John, "Strong localization of photons in certain disordered dielectric superlattices," Phys. Rev. Lett. 58 2486-2488, 1987

[3] J. D. Jounnaopoulos, R.D. Meade and J. N. Winn, "Photonic Crystals-Molding the Flow of Light", 1995

[4] Lord Rayleigh, Philosophical Magazine 24, 145-159, 1887

[5] Lord Rayleigh, Philosophical Magazine 26, 256-265, 1888

[6] Bong-Shik Song, Susumu Noda,* Takashi Asano, "Photonic Devices Based on In-Plane Hetero Photonic Crystals," Science 300, 1537-1537, 2003

[7] Toshitsugu Uesugi, Bong-Shik Song, Takashi Asano, and Susumu Noda, "Investigation of optical nonlinearities in an ultra-high-Q Si nanocavity in a two-dimensional photonic crystal slab," Opitics Express 14, 377-386, 2006

[8] A. Sharkawy, S. Shi, and D. W. Parther, "Band dropping via coupled photonic crystal waveguides," Opt. Express 10, 1279-1284, 2002

[9] M. Soljacic, S. G. Johnson, S. Fan, M. Ibannescu, E. Ippen, and J. D. Joannopoulos, "Photonic-crystal slow-light enhancement of nonlinear phase sensitivity" JOSA B, 19, 2052-2059, 2002

[10] M. Koshiba, "Wavelength Division Multiplexing and Demultiplexing With Photonic Crystal Waveguide Couplers," J. Lightwave Technol. 19, 1970-1975, 2001

[11] A. Sharkawy, S. Shi, and D. W. Parther, "Multichannel Wavelength Division Multiplexing with Photonic Crystals," Appl. Optics 40, 2247-2252, 2001

[12] M. Fujita, K. Ishihara, T. Ueno, T. Asano, S. Noda, H. Ohata, T. Tsuji, H. Nakada and N. Shimoji, "Optical and Electrical Characteristics of Organic Light-Emitting Diodes with Two-Dimensional Photonic Crystals in

Organic/Electrode Layers," J. J. Appl. Phys. 44, 3669-3677, 2005

[13] M. Notomi, K. Yamada, A. Shinya,1 J. Takahashi, C. Takahashi, and I. Yokohama, "Extremely Large Group-Velocity Dispersion of Line-Defect Waveguides in Photonic Crystal Slabs," Phys. Rev. Lett. 87, 253902 1-3, 2001

[14] R. Wilson, T. J. Karle, I. Moerman and T. F. Krauss, "Recirculation-enhanced switching in photonic crystal Mach-Zehnder interferometers," J. Opt. A: Pure Appl. Opt. 5, S76–S80, 2003

[15] Yu Tanaka, Y. Sugimoto, N. Ikeda, H. Nakamura, K. Asakawa,and K. Inoue, "Wavelength-Dependent Coupling Characteristics in Two-Dimensional Photonic-Crystal Slab Directional Coupler," J. J. Appl. Phys. 44, 4971–4974, 2005

[16] Dennis M. Sullivan, Electromagnetic Simulation Using the FDTD Method, 2000

[17] K. Lee, IEEE Transactions on Antennas and Propagation AP-14, 302-307, 1966

[18] E. P. Cunningham, Digital Filtering: An introduction, 1992

[19] A. V. Oppenheim and R. W. Schafer, Digital signal Processing, 1975

[20] S. Kuchinsky, V. Y. Golyatin, A.Y. Kutikov, T. P. Pearsall, and D. Nedeljkovic, "Coupling between photonic crystal waveguides," IEEE J. Quantum. ElEctron. 38, 1349-1352, 2002

[21] S. G. Johnson, S. Fan, P. R. Villeneuve, J. D. Joannopoulos, and L. A. Kolodziejski, "Guided modes in photonic crystal slabs," Physical Review B 60, 5751-5758 (1999)

[22] S. Boscolo, M. Kedrio, and C. G. Someda, "Coupling and Decoupling of Electromagnetic Waves in Parallel 2-D Photonic Crystal Waveguides," IEEE J. Quantum Electron. 38, 47-53 (2002)

[23] M. Thorhauge, L. H. Frandsen, and P. I. Borel, "Efficient photonic crystal directional couplers," Optics Letters 28 (17), 1525-1527 (2003)

[24] O. Painter, R. K. Lee, A. Scherer, A. Yariv, J. D. O'Brien, P. D. Dapkus, and I. Kim, "Two-Dimensional Photonic Band-Gap Defect Mode Laser," Science 284, 1819-1821 (1999)

[25] B. S. Song, S. Noda, T. Asano, and Y. Akahane, "Ultra-high-Q photonic double heterostructure nanocavity," Nature materials 4, 207-210 (2005)

[26] Y. Sugimoto, N. Ikeda, N. Carlsson, K. Asakawa, N. Kawai, and K. Inoue, "Light-propagation of Y-branch defect waveguide in AlGaAs-based air-bridge-type two-dimensional photonic crystal slabs," Optics Letter 27 (6), 388-390 (2002)

[27] S. Boscolo, M. Midrio, and T. F. Krauss, "Y-junctions in photonic crystal channel waveguides: high transmission and impedance match," Optics Letters 15 (27), 1001-1003 (2002)

[28] K. Inoue, Y. Sugimoto, N. Ikeda, Y. Tanaka, K. Asakawa, T, Maruyama, K. Miyashita, K. Ishida, and Y. Watanabe, "Ultra-Small GaAs-Photonic-Crystal-Slab-Waveguide-Based Near-Infrared Components: Fabrication, Guided-Mode Identification, and Estimation of Low-Loss and Broad-Band-Width in Straight-Waveguides, 60°-Bends and Y-Splitters," Japan Journal of Apply Physics 43 (9A), 6112-6124 (2004)

[29] M. Tokushima and H. Yamada, "Photonic crystal line defect waveguide directional coupler," Electro. Lett. 37 (24), 1454-1455 (2001)

[30] B. S. Song, S. Noda, and T. Asano, "Photonic Devices Based on In-Plane Hetero Photonic Crystals," Science 300, 1537-1537 (2003)

[31] N. Yamamoto, Y. Watanabe, and K. Komori, "Design of Photonic Crystal Directional Coupler with High Extinction Ratio and Small Coupling Length," Japan Journal of Apply Physics 44 (4B), 2575-2578 (2005)

[33] I. Park, H. S. Lee, H. J. Kim, K. M. Moon, S. G. Lee, B. H. O, S. G. Park, and E. H. Lee, "Photonic crystal power-splitter based on directional coupling," Optics Express 12 (15), 3599-3604 (2004)

[32] Y. Tanaka, H. Nakamura, Y. Sugimoto, N. Ikeda, K. Asakawa, and K. Inoue, "Coupling Properties in a 2-D Photonic Crystal Slab Directional Coupler With a Triangular Lattice of Air Holes," IEEE J. Quantum Electron. 41, 76-84 (2005)